

Identification of AGN in the *XMM-Newton* X-ray survey of the SMC [★]

★★

C. Maitra^{1***}, F. Haberl¹, V. D. Ivanov^{2,3} Maria-Rosa L. Cioni⁴, and Jacco Th. van Loon⁵

¹ Max-Planck-Institut für extraterrestrische Physik, Giessenbachstraße, 85748 Garching, Germany

² European Southern Observatory, Ave. Alonso de Crdova 3107, Vitacura, Santiago, Chile

³ European Southern Observatory, Karl-Schwarzschild-Str. 2, 85748 Garching bei München, Germany

⁴ Leibniz-Institut für Astrophysik Potsdam, An der Sternwarte 16, 14482 Potsdam, Germany

⁵ Lennard-Jones Laboratories, Keele University, ST5 5BG, UK

Preprint online version: October 30, 2018

ABSTRACT

Context. Finding Active Galactic Nuclei (AGN) behind the Magellanic Clouds (MCs) is difficult because of the high stellar density in these fields. Although the first AGN behind the Small Magellanic Cloud (SMC) were reported in the 1980s, it is only recently that the number of AGN known behind the SMC has increased by several orders of magnitude.

Aims. The mid-infrared colour selection technique has been proven to be an efficient means of identifying AGN, especially obscured sources. The X-ray regime is complementary in this regard and we use *XMM-Newton* observations to support the identification of AGN behind the SMC.

Methods. We present a catalogue of AGN behind the SMC by correlating an updated X-ray point source catalogue from our *XMM-Newton* survey of the SMC with already known AGN from the literature as well as a list of candidates obtained from the ALLWISE mid-infrared colour selection criterion. We studied the properties of the sample with respect to their redshifts, luminosities and X-ray spectral characteristics. We also identified the near-infrared counterpart of the sources from the VISTA observations.

Results. The redshift and luminosity distributions of the sample (where known) indicate that we detect sources from nearby Seyfert galaxies to distant and obscured quasars. The X-ray hardness ratios are compatible with those typically expected for AGN. The VISTA colours and variability are also consistent in this regard. A positive correlation was observed between the integrated X-ray flux (0.2–12 keV) and the ALLWISE and VISTA magnitudes. We further present a sample of new candidate AGN and candidates for obscured AGN. All of these make an interesting subset for further follow-up studies. An initial spectroscopic follow-up of 6 out of the 81 new candidates showed all six sources are active galaxies, albeit two with narrow emission lines.

Key words. Magellanic Clouds – quasars: general – X-rays: galaxies – infrared: galaxies – catalogues

1. Introduction

Active galactic nuclei (AGN) are amongst the most powerful and steady sources of luminosity in the universe ranging from AGN in nearby galaxies emitting at luminosities about 10^{40} erg s⁻¹, to distant quasars emitting $> 10^{47}$ erg s⁻¹. AGN play a crucial role in the formation and evolution of galaxies (e.g. Caputi 2014), and in the growth of supermassive black holes (Fabian & Iwasawa 1999).

Identification of AGN behind the Magellanic Clouds (MCs) can be a challenging task, because of the high stellar density in these fields. The first small samples of quasars behind the Small Magellanic Cloud (SMC) were reported in the 1980s (Mills et al. 1982; Wilkes et al. 1983). Tinney et al. (1997) confirmed eight new sources by performing optical spectroscopic follow-up of *ROSAT* X-ray sources. Further, Dobrzycki et al. (2003b,a) and Geha et al. (2003) identified five candidates from X-ray selection and five using the optical variability properties from the

Magellanic Cloud OGLE-II data (Eyer 2002). The Magellanic Quasar Survey (MQS) played a significant role in increasing the number of AGN behind the MCs. In the first work of a series, Kozłowski & Kochanek (2009) selected 657 candidates using *Spitzer* space telescope in the infrared and near-infrared photometry. Subsequently, based on the candidates from Kozłowski & Kochanek (2009), and additional ones selected by optical variability from OGLE data together with mid-IR and/or X-ray properties, Kozłowski et al. (2011, OGLE-II) and Kozłowski et al. (2013, OGLE-III) were able to confirm 193 of the 766 candidates selected in total by performing follow-up spectroscopy.

The last years have witnessed an increase in the number of identified AGN by several orders of magnitude. A large fraction of this owes to the advent of the mid-infrared colour selection technique which has proven to be a very efficient means of identifying AGN. This technique is based on detecting the hot obscured dust surrounding an AGN, which is much less affected by extinction. For the same reason this method is also effective in finding the most obscured AGN, and is in a way complementary to X-ray surveys of AGN at energies < 10 keV which are only partially sensitive to Compton-thick AGN ($N_H > 10^{24}$ cm⁻²; Della Ceca et al. 2008). The mid-infrared selection techniques have been introduced by Lacy et al. (2004), Stern et al. (2005) and Donley et al. (2012) using data from the *Spitzer* mission. This was later adapted for the Wide-field Infrared Survey

* Based on observations with *XMM-Newton*, an ESA Science Mission with instruments and contributions directly funded by ESA Member states and the USA (NASA)

** Based on observations made with VISTA at the Paranal Observatory under programme ID(s) 179.B-2003(G), 179.B-2003(F), 179.B-2003(D), 179.B-2003(C), 179.B-2003(H), 179.B-2003(B)

*** e-mail: cmaitra@mpe.mpg.de

Explorer (*WISE*; Wright et al. 2010) mission which performed an all-sky survey in the infrared bands at 3.4, 4.6, 12 and 22 μm . The mission achieved 5σ point source sensitivities better than 0.08, 0.11, 1 and 6 mJy at 3.4, 4.6, 12 and 22 μm respectively, with angular resolutions of 6.1, 6.4, 6.5 and 12'' in the respective bands. Stern et al. (2012); Assef et al. (2013) applied one colour selection criterion using 3.4 and 4.6 μm wavebands from the ALLWISE data to select AGN. Mateos et al. (2012) formulated a more advanced and effective two-colour wedge selection criterion of these sources. All of the selection criteria are based on the fact that the AGN separate cleanly from stars and star forming galaxies in the mid-infrared colour space.

Based on this, Secrest et al. (2015) presented an all-sky catalogue of 1.4 million AGN selected using the two-colour mid-infrared criteria for AGN (Mateos et al. 2012), applied to sources from the *WISE* final catalogue release (ALLWISE). This included approximately 1.1 million previously uncatalogued AGN. Additionally, the Half-Million Quasars catalogue (HMQ) (Flesch 2015) lists a sample of 510,764 objects. This included high confidence SDSS based photometric quasars with radio/X-ray associations as well as BL Lac and type 2 objects with accurate source positions. Recently, Flesch (2017) published the Million Quasars (MILLIQUAS) catalogue, which is an updated version of the former catalogue including $\sim 900\text{k}$ high-confidence quasar candidates from SDSS-based photometric quasar catalogues and also from all-sky radio/X-ray associated objects, bringing the total count to 1,422,219. However only a small fraction of this catalogue contained X-ray selected sources or sources with X-ray associations.

The *XMM-Newton* survey of the SMC (Haberl et al. 2012) provided the deepest complete coverage of the main body of the SMC (bar and eastern wing, $\sim 5.58 \text{ deg}^2$) in the X-ray (0.2–12.0 keV) band. The bulk ($>71\%$) of the 3053 X-ray-emitting point sources that were detected are expected to be AGN although only 72 could be identified with high confidence (Sturm et al. 2013b). This is because, for an individual faint ($\sim 10^{-14} \text{ erg cm}^{-2} \text{ s}^{-1}$) X-ray source, it is difficult to prove the AGN nature. Moreover, owing to the coordinate uncertainties of an *XMM-Newton* source (typical $\sigma \sim 1''.2$, after astrometric correction), it is challenging to find the optical counterpart because of the high density of SMC stars, which causes chance coincidences with typically up to ~ 4 optical sources. Sturm et al. (2013a) used associations of the X-ray point sources with radio emission to effectively select 43 new candidates for AGN behind the SMC. With the large database of all-sky quasar catalogues available now, and additional effective selection methods in other wavebands (especially in the mid-infrared) well tested, we have now the ideal opportunity to identify many more quasars behind the SMC.

AGN behind the MCs are particularly important for two additional reasons. First, they are ideally suited as anchors for an absolute astrometric reference system for proper motion studies (e.g. Kallivayalil et al. 2013; Cioni et al. 2014). Also in the context of X-ray sources, we note the importance of having identified X-ray sources to improve the astrometric quality of X-ray catalogues in the field of the MCs. The brightest sources might be used to probe absorption by the interstellar medium in the MCs. Finally, the AGN can be the subject of investigations using the comprehensive multi-epoch and multi-wavelength data available for the MCs (e.g. Kelly et al. 2009).

In this paper we present a catalogue of X-ray detected AGN behind the SMC by correlating an updated point source catalogue of the *XMM-Newton* SMC survey with lists of AGN known from literature and of candidates obtained in this work using the ALLWISE mid-infrared colour selection criterion. In

Sect. 2 we describe the observations, the data reduction and the production of the AGN samples based on mid-infrared selections and from published catalogues and their correlation with the X-ray data. In Sect. 3 we describe the results and characterise the selected AGN. In Sect. 4 we present a summary and conclusions. For calculation of luminosities, we adopted the standard cosmological parameters: $\Omega_M = 0.3$, $\Omega_A = 0.7$ and $H_0 = 70 \text{ km s}^{-1} \text{ Mpc}^{-1}$.

2. Observations and data reduction

2.1. X-ray data and the updated SMC survey

The *XMM-Newton* (Jansen et al. 2001) survey of the SMC (Haberl et al. 2012) provided the deepest complete coverage of the main body of the SMC (bar and eastern wing, $\sim 5.58 \text{ deg}^2$) in the 0.2–12.0 keV band. Using additional outer fields, a catalogue of 3053 X-ray point sources was created. A detailed description of the catalogue and the used observations are presented in Sturm et al. (2013b). We added to this sample new observations of the SMC wing region acquired as part of the SMC Wing survey (PI: F. Haberl), and all observations publicly available up to satellite revolution 3177 (2017-04-14). This resulted in 44 new pointings (including archival observations). The updated survey has a total exposure of 3.4 Ms and covers an area of $\sim 6.67 \text{ deg}^2$ and will be described in detail in a forthcoming paper. The new observations are listed in Table 1. We reprocessed the entire dataset mentioned above in the same way as for the SMC X-ray point-source catalogue using the latest version of SAS (16.1), also including new boresight corrections utilising the catalogue of AGN compiled from this work. In contrast to Sturm et al. (2013b) we applied background filtering individually to each instrument. This resulted in a gain of exposure times for MOS1 and MOS2 in most cases. For the compilation of the updated SMC point source catalogue we applied a reduced systematic error of $0''.33$ in comparison to Sturm et al. (2013b) who used a value of $0''.5$. This is comparable to the systematic error applied to the 3XMM-DR6 catalogue (Rosen et al. 2016)¹. A total of 8690 detections were found from the entire SMC survey area, which include detections with detection likelihood of ≥ 6 . Unique sources were included in the catalogue when at least one detection was found with a detection likelihood of ≥ 10 . This resulted in 4449 unique X-ray point sources. The master source positions and the corresponding errors were calculated from the error-weighted average of the individual detections. All the sources identified in this work were screened individually by visual inspection to avoid spurious detections.

2.2. The mid infrared sample & the ALLWISE data

We selected all sources from the ALLWISE catalogue within a radius of 3.33° around R.A. = $01^{\text{h}}00^{\text{m}}00^{\text{s}}$, Dec. = $-72^\circ30'00''$ (area of the *XMM-Newton* SMC survey) following the two-colour selection criterion of Mateos et al. (2012, see eqn. 3 and 4). We additionally imposed a requirement that the selected sources have a signal-to-noise-ratio $S/N \geq 3$ in all the three bands of selection (3.4, 4.6 and 12 μm : W1, W2 and W3 from now) and are unaffected by known artifacts (cc_flags == '0000'). This implied the same criteria as used by Secrest et al. (2015)

¹ After resolving a known problem in coordinate conversion from SAS 15.0 onwards, a better agreement between the X-ray and optical positions were obtained. See <https://www.cosmos.esa.int/web/xmm-newton/sas-release-notes-1500>

Table 1: New *XMM-Newton* observations since Sturm et al. (2013b) given in chronological order.

ObsID	R.A.	Dec.	Exp _{pn}	Exp _{m1}	Exp _{m2}	Δ R.A.	Δ Dec.
0412981301	01:04:22.48	-72:01:10.8	2873	21683	22730	1.197	0.659
0677980301	01:01:37.89	-72:25:28.4	5233	9433	11050	-0.479	0.019
0412981401	01:03:42.98	-72:01:29.2	28721	32744	33634	-2.062	-0.247
0679180301	00:23:52.40	-72:23:09.3	9538	14103	14576	–	–
0412981501	01:04:26.97	-72:00:52.6	0	29924	29929	-0.878	-0.115
0412981601	01:02:07.05	-71:55:32.2	0	0	28715	0.384	-0.151
0700381801	01:28:05.26	-73:31:59.6	29880	31458	31463	0.106	0.362
0693050501	01:23:20.21	-75:21:21.2	9449	13621	14128	1.670	0.632
0412981701	01:04:09.40	-72:01:02.2	47095	56783	43900	-0.375	-1.010
0721960101	01:28:03.92	-73:31:51.2	70282	77693	78552	1.521	0.264
0724650301	01:33:15.19	-74:25:01.8	22628	33114	33621	0.857	1.387
0700580101	00:57:06.59	-72:24:37.3	8847	13449	13419	0.151	-1.199
0412982101	01:04:08.95	-72:00:44.6	30371	31953	31923	0.039	-1.102
0700580401	00:57:22.99	-72:26:09.6	14005	19277	19451	0.547	-0.777
0700580601	00:57:18.04	-72:25:24.1	16377	18646	18619	-0.002	-0.452
0674730201	00:59:00.25	-71:40:09.0	19199	19395	19303	–	–
0412982301	01:04:24.13	-72:01:40.5	43350	43533	43508	2.898	-0.837
0412982201	01:04:09.51	-72:00:44.4	32418	33596	33624	0.970	-0.209
0741450101	01:25:40.47	-73:17:59.2	49673	50199	76693	-0.433	-1.783
0770580701	00:54:50.45	-73:39:49.4	0	9650	9355	2.211	-1.208
0770580801	00:54:51.89	-73:39:58.8	28080	28395	28397	1.012	-0.183
0764780201	00:43:02.49	-73:39:45.3	46365	47950	47921	0.311	-0.977
0770580901	00:54:54.88	-73:40:22.9	20395	22027	23663	0.600	-3.385
0764050101	00:54:19.22	-72:29:45.3	13141	26649	26619	0.057	0.585
0412982501	01:04:23.44	-72:01:36.4	33362	33535	33524	-0.104	-0.053
0412982401	01:04:09.37	-72:00:45.4	32993	35803	36770	0.743	-0.315
0763590401	01:22:03.92	-72:57:08.2	21034	23543	23515	0.022	1.810
0764050201	00:53:40.14	-72:31:28.4	17667	30099	33086	-0.276	-0.654
0791580701	01:03:40.16	-72:02:17.0	30475	30651	30611	-0.513	0.615
0791580801	01:03:40.12	-72:02:18.0	12128	12655	12615	-0.498	0.240
0791580901	01:03:40.03	-72:02:17.4	11777	12603	12615	-0.803	0.579
0791581001	01:03:40.12	-72:02:18.2	30477	30655	30615	-0.454	-0.287
0791581101	01:03:40.13	-72:02:18.1	13815	14292	14258	-0.560	-0.511
0791581201	01:03:40.04	-72:02:17.1	350	14973	15659	-1.040	0.113
0784690601	01:29:13.99	-73:07:54.7	30337	34546	34620	-1.723	-1.465
0784690701	01:23:14.81	-73:29:11.7	27660	32846	33187	1.822	0.537
0784690401	01:19:18.91	-73:39:47.7	24747	37517	37664	1.380	-0.545
0412983201	01:04:09.26	-72:00:46.7	29216	33323	33400	0.989	-1.236
0784690801	01:33:12.21	-73:17:02.4	38141	41388	41619	1.142	-0.077
0784690201	01:12:38.71	-73:28:14.2	29605	36502	37609	-0.135	-1.117
0412983301	01:04:23.86	-72:01:49.2	29036	33585	33617	0.996	1.362
0784690101	01:09:32.19	-73:19:19.2	22309	27317	28281	2.955	1.665
0784690301	01:15:02.69	-73:43:27.9	38684	40282	40259	-0.144	-1.854
0803210201	01:07:23.59	-72:28:27.2	33739	35649	35621	-0.588	0.326

Notes. Coordinates are in J2000. Net exposures for all EPIC instruments are given in s. Δ R.A. and Δ Dec denote the shifts in R.A. and Dec. after boresight correction in arcsec. For the observation log of the *XMM-Newton* SMC catalogue, see Table B.1 of Sturm et al. (2013b). Observations starting with 04129 correspond to routine calibration observations of 1ES0102–72 and 07846 to the SMC wing survey.

albeit with a more relaxed S/N requirement of 3 instead of 5. Secrest et al. (2015) adopted a criterion of $S/N \geq 5$ in order to minimise the contamination from star-forming galaxies. However, the presence of a corresponding X-ray counterpart of an ALLWISE source makes this less likely. The relaxed S/N criterion enabled us to increase our sample of detected AGN, while our choice of mid-infrared colour selection is well suited to also find AGN behind highly obscured regions of the SMC.

2.3. HMQ/MILLIQUAS catalogues

In order to find more sources for the reference AGN sample that were either not detected in the ALLWISE data, or did not have the colours matching the Mateos et al. (2012) criterion, we

selected additional high confidence sources with known spectroscopic redshifts from the HMQ and the MILLIQUAS catalogue within the area of the *XMM-Newton* SMC survey. This resulted in a total of 2753 sources from the ALLWISE data and the HMQ/MILLIQUAS, out of which 2587 (94%) are from the ALLWISE data.

2.4. Correlation of the *XMM-Newton* and ALLWISE/HMQ/MILLIQUAS catalogues

In order to identify the AGN behind the SMC from the survey data, we cross-correlated the X-ray and the ALLWISE/HMQ/MILLIQUAS samples described in the previous subsections. For the cross-match we used TOPCAT v 4.2–

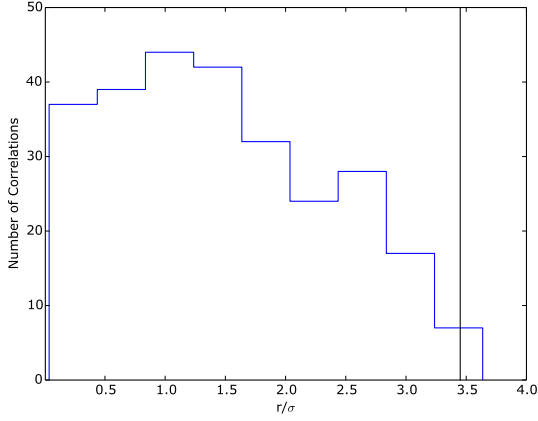


Fig. 1: Distribution of uncertainty-normalised angular separations for 276 *XMM-Newton* correlations with the total AGN sample of 2753 sources. For real counterparts, we expect a Rayleigh distribution. The vertical line indicates the 99.7% completeness.

l^2 , and adopted the following selection methods to optimise the purity of the resulting sample. Sources with uncertain X-ray coordinates can result in more than one match, which is therefore insecure. In the following, we only used X-ray sources with a 1σ position uncertainty of $\sigma_X < 2''.5$ (4311 out of 4449 sources). We further regarded all correlations with an angular separation of

$$r \leq 3.439 \times \sqrt{\sigma_X^2 + \sigma_{\text{MIR/HMQ/MILLIQUAS}}^2} = 3.439\sigma.$$

For a Rayleigh distribution this corresponds to a 99.7% completeness. The typical position accuracy of an X-ray source is $1''.2$. The ALLWISE position uncertainties are $< 1''$ for all sources and better than $0''.15$ for high S/N sources (Wright et al. 2010). The coordinate uncertainties of the HMQ/MILLIQUAS sample is $\sim 0''.2$. Fig. 1, shows the distribution of the uncertainty normalised angular separation between the correlated sources after applying the criteria described above.

To estimate the probability of chance coincidence, we cross-correlated the X-ray sample with the total sample of AGN by shifting the coordinates of the latter by large offsets ($3'$ in either R.A. or Dec.). We estimate the probability of chance coincidence to be 0.003%.

3. Results and discussion

3.1. The X-ray selected sample: characterisation

We found a total of 276 X-ray sources uniquely correlating with the selected sample of AGN (Table A.6). Out of them 218 in total were selected using the ALLWISE selection criteria, with 81 new AGN candidates identified from this work, and 137 already classified as AGN by Secrest et al. (2015) (Table 2). The rest (58) were selected exclusively from the MILLIQUAS and the HMQ catalogue. The spatial distribution of the sample (Fig. 2), shows that the identified AGN are scattered uniformly within the *XMM-Newton* survey area with no particular spatial dependence on the selection criteria (ALLWISE/HMQ/MILLIQUAS) used for the sample.

3.1.1. Redshift

From the 276 sources, 90 have their redshifts (z) determined. Their distribution is shown in Fig. 3, right. The median z of the sample is 1.06, the lowest is 0.07 (classified as a Seyfert galaxy 6dFGS gJ005356.2–703804) and the highest is 2.878 (classified as quasar SMC J010127.75–721306.2). This indicates that we detect sources with a wide range of z from nearby Seyfert galaxies to distant quasars. We detected 14 objects with high redshifts ($z \geq 2$). Although most of the sample was selected by correlating the X-ray source list with the ALLWISE mid-infrared two colour selection, only 29 of the objects with known z are from the ALLWISE sample. This is consistent with the fact that out of the 2587 sources identified within the area of the *XMM-Newton* survey that satisfied the criterion of Mateos et al. (2012), only 73 contain redshift information. The rest was selected from the MILLIQUAS and the HMQ catalogue. Moreover, all the sources with $z \geq 2$ were also selected from the MILLIQUAS and the HMQ catalogue. We verified that the high z sources were distributed randomly within the survey area of the SMC, further indicating that there is no dependence of the selection criteria used for identification of the sources on the area of the survey.

3.1.2. Flux and luminosity

We calculated the average X-ray flux for each source of the sample (0.2–12 keV) by converting the count rates using conversion factors taken from Sturm et al. (2013b). This assumes a power-law model with a photon index of 1.7 and a photo-electric foreground absorption by the Galaxy of $6 \times 10^{20} \text{ cm}^{-2}$ (average for the SMC main field in the HI map of Dickey & Lockman 1990). The flux of the sample has a median at $7.0 \times 10^{-14} \text{ erg cm}^{-2} \text{ s}^{-1}$ (Fig. 3, left). The minimum flux detected in the sample is $6.0 \times 10^{-15} \text{ erg cm}^{-2} \text{ s}^{-1}$, which is near the sensitivity limit of the survey. The highest flux detected is $5.0 \times 10^{-12} \text{ erg cm}^{-2} \text{ s}^{-1}$ from a nearby object ($z = 0.074$).

For the sources with known z , we determined the rest-frame X-ray luminosities (0.2–12 keV). The X-ray luminosity distribution is shown in Fig. 4, left. The median of the sample is $1.9 \times 10^{44} \text{ erg s}^{-1}$ and the minimum luminosity determined is $3.7 \times 10^{42} \text{ erg s}^{-1}$. The lower limit of our sample is compatible with the value at which the AGN luminosity dominates over the host galaxy emission and can be selected effectively using AGN colour selection criteria (Stern 2015, and references therein). We note however, that the luminosities were calculated using the flux obtained from converting the count rates alone, and were not corrected for obscuration effects due to local or the line-of-sight absorption. Hence it does not reflect the intrinsic luminosity of the sample. In order to obtain a robust estimation of the true luminosity, we determined the $6\mu\text{m}$ rest-frame luminosity for the 29 sources containing information on the magnitudes in the four ALLWISE bands (3.4, 4.6, 12 and $22 \mu\text{m}$, Mountrichas et al. 2017). The choice of the wavelength was motivated by the fact that $6 \mu\text{m}$ provides an unbiased estimate of the bolometric luminosity representing the torus luminosity. Further, the contribution from star-formation is negligible at this wavelength (Mountrichas et al. 2017). Figure 4, right shows the distribution of the infrared luminosity (in red) and the X-ray luminosity (in blue) for the sample. The median of the infrared-luminosity (νL_ν) distribution is $4.7 \times 10^{46} \text{ erg s}^{-1}$ and the highest determined value is $3.2 \times 10^{47} \text{ erg s}^{-1}$ (indicative of a powerful quasar).

Figure 5 shows the comparison of the rest-frame X-ray (0.2–12 keV, not corrected for absorption) and the mid-infrared ($6 \mu\text{m}$) luminosity of this sample. Previous works in this regard

² <http://www.star.bris.ac.uk/mbt/topcat/>

Table 2: AGN behind the SMC selected in this work.

Reference	Number of sources	Comments
Secrest et al. (2015)	137	29 also included in HMQ/MILLIQUAS
HMQ/MILLIQUAS	58	None in ALLWISE
New candidates	81 (Table A.1)	selected by relaxing the S/N criterion in the ALLWISE data 59 catalogued as AGN candidates for the first time

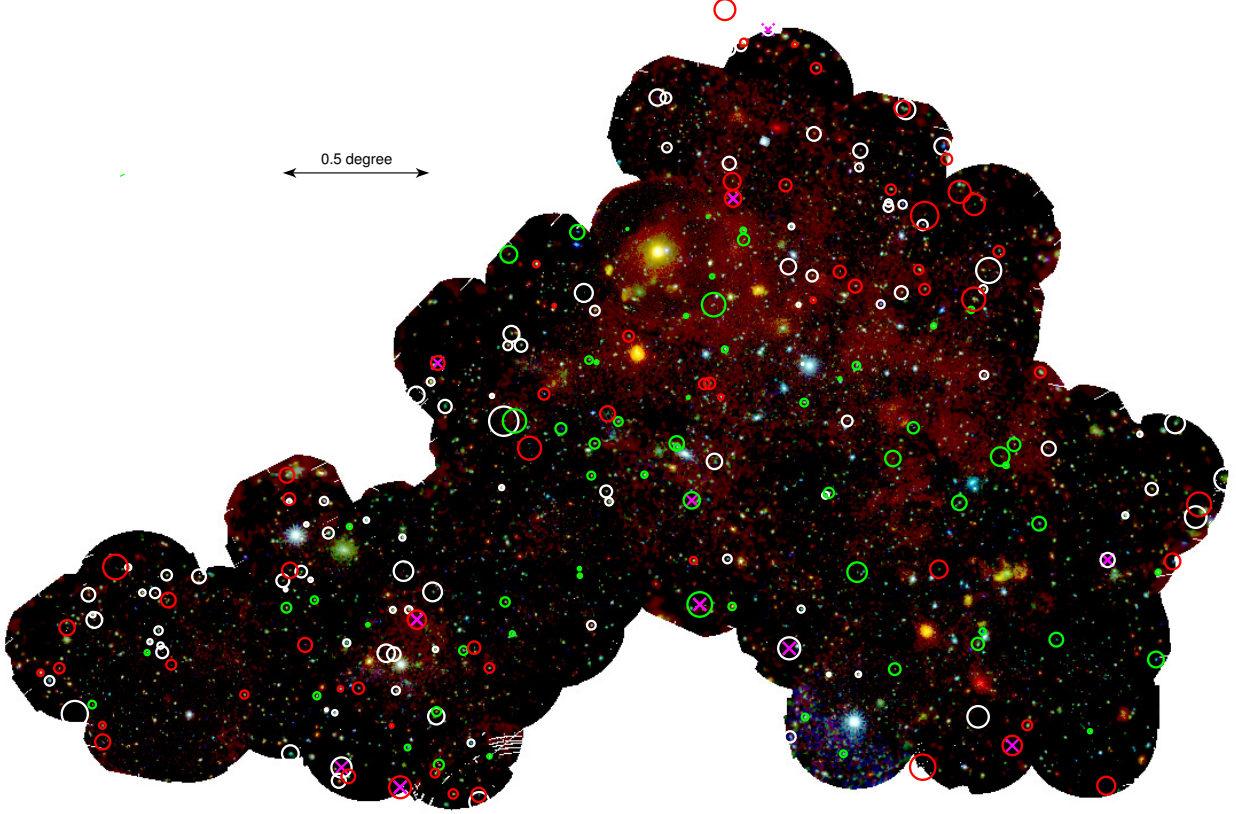


Fig. 2: Mosaic image of all *XMM-Newton* observations used in the updated SMC survey. Red/green/blue: 0.2–1.0 / 1.0–2.0 / 2.0–4.5 keV intensities. White circles denote the sources selected from Secrest et al. (2015), green circles those from the HMQ and MILLIQUAS survey (Flesch 2015, 2017), and red circles mark the 81 new AGN candidates which we identified. The magenta crosses indicate the candidates for obscured AGN. The circle radius is scaled with the uncertainty on the X-ray positions.

have demonstrated how the luminosities are correlated (Gandhi et al. 2009; Fiore et al. 2009; Lanzuisi et al. 2009), including Stern (2015) who formulated the global X-ray to mid-IR relation of AGN which is appropriate for a large range of luminosities from Seyfert galaxies to luminous quasars. Figure 5 shows that the brightest objects in mid-IR are also bright in X-rays. To quantify the correlation, we determined the Kendall’s τ rank correlation coefficient to be 0.70. Artificial correlations may be introduced between luminosities due to the effect of redshift in a flux-limited sample. In order to take this into account, we determined the partial Kendall’s τ rank correlation coefficient to be 0.44, indicating a weaker intrinsic correlation between the X-ray and mid-IR luminosities.

We also compare our results with the X-ray to mid-IR relation of AGN. The X-ray luminosities determined in this work are systematically lower than predicted by the relation. The bias

indicates the presence of significant X-ray obscuration. This is because the formulation of Stern (2015) is based on absorption corrected luminosities in the energy band of 2–10 keV. The X-ray luminosities reported in this work on the other hand are obtained from converting count rates to average flux (0.2–12 keV), and accounting only for a photo-electric foreground absorption by the Galaxy of $6 \times 10^{20} \text{ cm}^{-2}$. As the AGN are distributed uniformly within the *XMM-Newton* survey area (Fig. 2), an additional obscuration of $N_{\text{H}} = 2 \times 10^{21} \text{ cm}^{-2}$ through the depth of the SMC (as is typically found in the wing region of the SMC; Stanimirovic et al. 1999) corresponds to an increase in the absorption-corrected luminosity of $\sim 2\%$ in the 2–10 keV energy range and 15% in the 0.2–12 keV range. Similar factors corresponding to $N_{\text{H}} = 10^{22} \text{ cm}^{-2}$ (as is typically found in the bar region of the SMC; Stanimirovic et al. 1999) are 8% and 30% respectively. We performed a least-square polynomial fit to

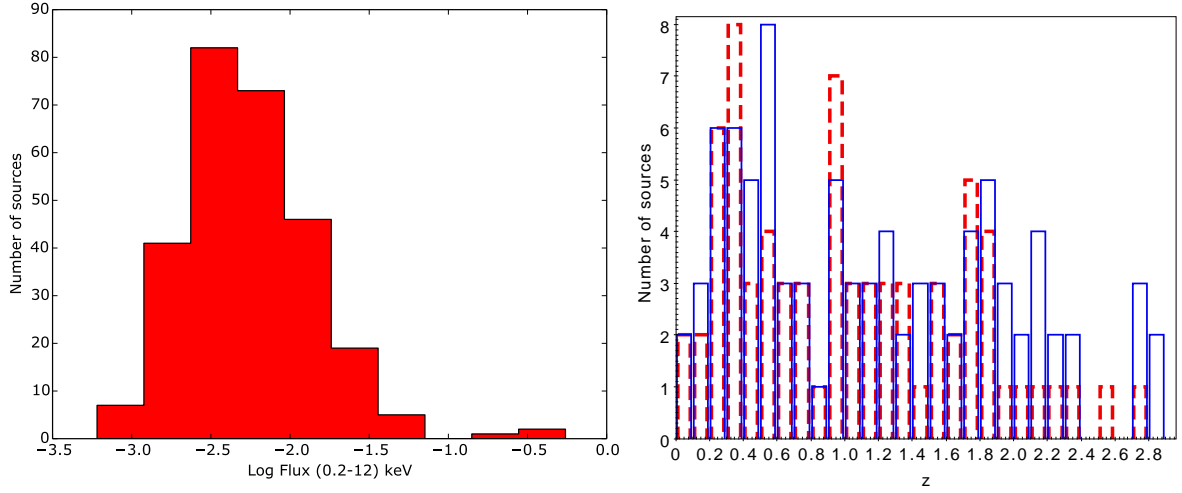


Fig. 3: *Left*: X-ray flux (in units of $10^{-11} \text{ erg cm}^{-2} \text{ s}^{-1}$ in the energy range of 0.2–12 keV) distribution of the sample; *Right*: Redshift distribution of the sample where known (in red) and redshift distribution of all AGN with known z (in blue) within the *XMM-Newton* SMC survey from Secrest et al. (2015).

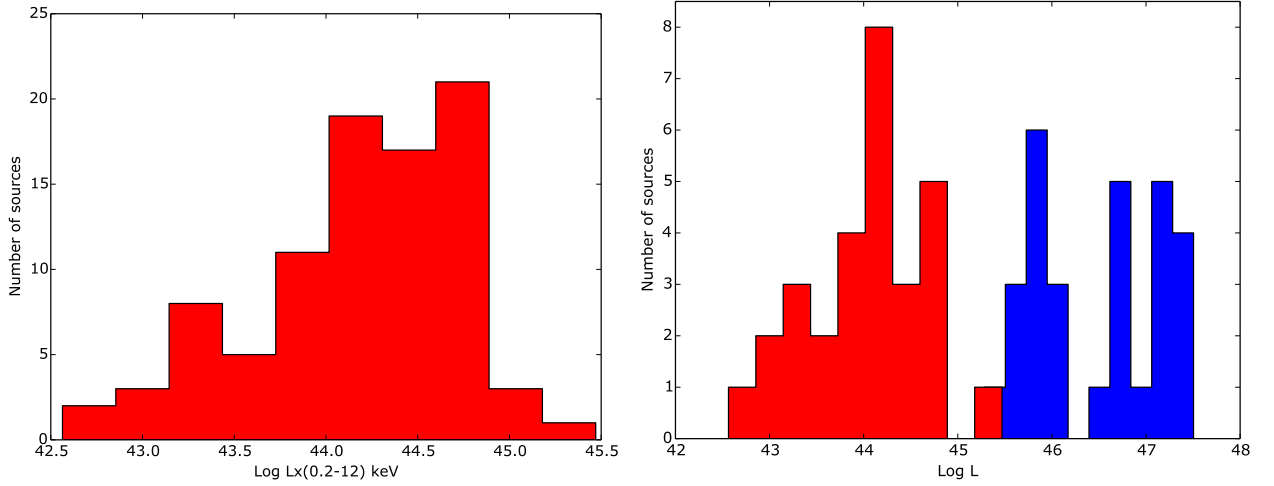


Fig. 4: *Left*: X-ray luminosity (in units of erg s^{-1}) distribution of the sub-sample with known redshift; *Right*: Comparison between X-ray (red) and mid-infrared (blue) luminosity distribution from a smaller set where both the X-ray and mid-infrared luminosities can be determined.

the data and derived a slightly different relation (not corrected for absorption) than Stern (2015):

$$\log L_x(0.2 - 12 \text{ keV}) = 37.711 + 1.455x - 0.042x^2,$$

where L_x is in units of erg s^{-1} and $x \equiv \log(\nu L_\nu / 10^{41} \text{ erg s}^{-1})$. A change in slope of our obtained relation as compared to the global formulation of Stern (2015) indicates that the intrinsic absorption of the AGN is an important contributing factor to the total absorption component. As the AGN intrinsic absorption is redshift dependent, it would have a higher effect on nearby, low luminosity Seyfert galaxies as compared to luminous and distant quasars in the observers reference frame.

3.1.3. X-ray Spectral characteristics

The X-ray spectra of an AGN can typically be described by a power law with photon index of $\Gamma \sim 1.75$ (e.g. Tozzi et al. 2006) and therefore show a hard X-ray spectrum compared to Galactic stars. As shown by Sturm et al. (2013b), hard X-ray sources can

be selected efficiently using the hardness-ratio relation

$$8HR_2 + 3HR_3 > -3$$

or sources with $HR_2 > 0$ if HR_3 is not defined, due to lack of statistics. Here, hardness ratios are derived by comparing count rates in neighbouring *XMM-Newton* energy bands: $HR_i = (R_{i+1} - R_i) / (R_{i+1} + R_i)$, where $i=1$ for 0.2–0.5 keV, $i=2$ for 0.5–1.0 keV, $i=3$ for 1.0–2.0 keV, $i=4$ for 2.0–4.5 keV and $i=5$ for 4.5–12.0 keV. We extracted this information for the AGN sample and plotted the HR_2 – HR_3 hardness–hardness diagram as shown in Fig. 6. We found that almost all the sources (except a few with very large error bars) lie within the specified region for AGN in the HR_2 – HR_3 plane prescribed in Sturm et al. (2013b). This further validated the robustness of our selection.

The mid-infrared based surveys have the potential to find the most obscured and even Compton-thick AGN ($N_H \geq 10^{24} \text{ cm}^{-2}$), and thus helps in identifying X-ray selected heavily obscured AGN (Secrest et al. 2015, and references therein). This motivated us to look for obscured AGN within the sample. Brightman

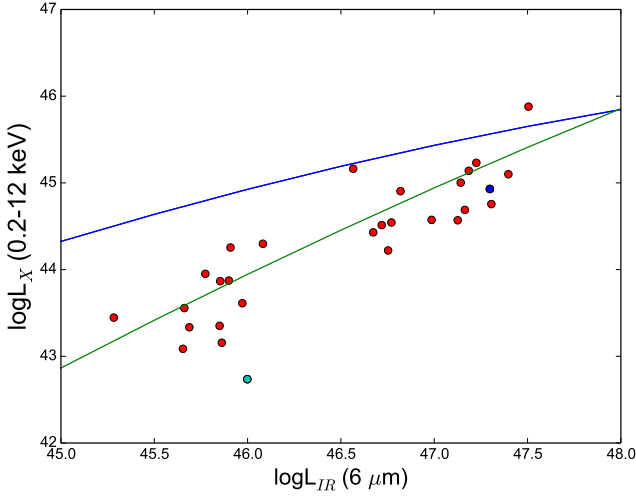


Fig. 5: Comparison of X-ray (0.2–12 keV) and mid-infrared (6 μm) luminosity (in units of erg s^{-1}) shown in Fig. 4. The blue line denotes the X-ray-mid-IR luminosity relation from Stern (2015). The blue dot marks the candidate for obscured AGN identified by comparing the X-ray hardness-ratio of the sample. The cyan dot marks the candidate for obscured AGN identified from an unusually low L_X/L_{IR} ratio. The green line denotes the relation derived from this work for the current sample.

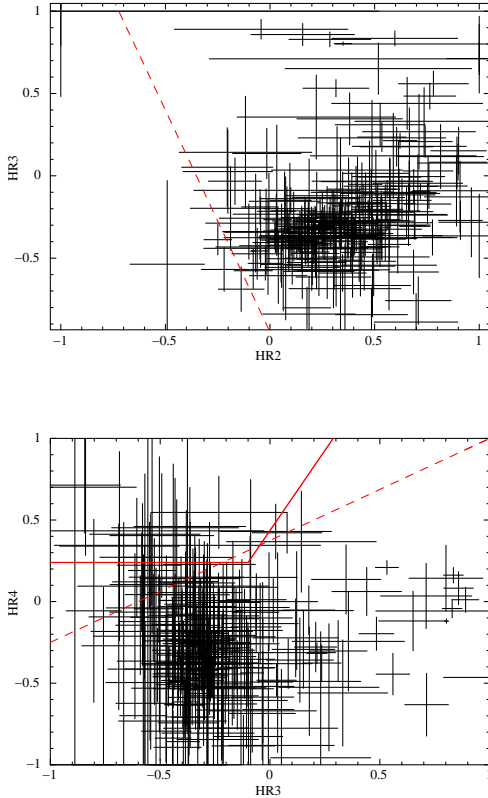


Fig. 6: *Top*: Hardness ratio diagram for the AGN sample. The dashed line defines the spectral classification criterion in HR3 vs. HR2 by Sturm et al. (2013b) to identify AGN. *Bottom*: Hardness ratio diagram as the top figure, albeit in different energy bands. The solid wedge and the dashed line defines the selection criteria for highly obscured AGN in Brightman & Nandra (2012).

& Nandra (2012) showed that heavily obscured sources can be well separated in X-rays by being hard in the band HR2 (\equiv to HR4 band in our definition) and soft in HR1 (\equiv to HR3 band in our definition). Using equation (1) and (2) from Brightman & Nandra (2012), we found that 13 sources satisfy the criteria of expected $N_H \geq 10^{24} \text{ cm}^{-2}$ (Compton-thick) and 20 sources satisfy the criteria of expected $N_H \geq 10^{23} \text{ cm}^{-2}$ (see Fig. 6 and Table A.4). Alternatively, an unusually low L_X/L_{IR} ratio has been used to test the Compton-thick nature of candidates in nearby ($z < 0.1$) AGN (Severgnini et al. 2012; Rovilos et al. 2014). With this approach we found one more candidate by looking for extreme outliers in the X-ray to mid-IR luminosity comparison (source marked cyan in Fig. 5). All the 21 sources were distributed evenly within the survey area, except the bar region of the SMC, where the absorption within the SMC is the highest (see Fig. 2). This is further indicative of the fact that the sources are intrinsically absorbed. The high absorption in the bar region also makes the X-ray detection of the obscured AGN difficult. Interestingly, for three of these sources $z \sim 2$, which is indicative of distant objects. The possible luminous, distant and obscured quasar candidates are rare objects, and their identification is crucial to reproduce the shape of the cosmic X-ray background (see for instance Gilli et al. 2007). These sources therefore deserve attention for further follow-up studies. The sample of possibly obscured AGN also contains 8 newly identified candidates described in section 3.2. The fraction of Compton-thick AGN candidates constitute $\sim 5\%$ of the total sample and is roughly consistent with the fraction detected in the *XMM-Newton* survey of the COSMOS field (Hasinger et al. 2007) and the Lockman hole (Hasinger et al. 2001).

To confirm their nature, it would be ideal to investigate the X-ray spectra of the sample to constrain the N_H , determine the unabsorbed X-ray luminosities of the sources, or look for signatures of obscured AGN such as a convex-shaped X-ray spectrum indicative of very high N_H or a Fe-K emission line of high equivalent width (see e.g. Terashima et al. 2015). All the sources were however either detected off-axis and/or are X-ray faint. Therefore, the statistical quality of the source spectra were inadequate for performing a meaningful analysis. The identified sources are nevertheless promising targets for follow-up studies of distant obscured quasars.

3.2. Correlation with the SMC X-ray point source catalogue from 2013

We correlated our sample with the SMC point source catalogue of Sturm et al. (2013b) which is based on a subset of the observations used for this work. We found that 201 of our 276 sources are included in that catalogue. Forty of them were already classified as AGN. The remaining sources were either unclassified or candidate AGN. Our work further validates the candidate sources as real AGN. Only 8 out of the selected sources were included in the sample of 88 AGN with radio associations (Sturm et al. 2013a). We note that although 12 more out of the 88 sources had a counterpart in the ALLWISE catalogue, their mid-infrared colours did not meet the selection criterion of Mateos et al. (2012). The very small overlap between the sample selected from radio associations, and the present selection methods indicate that they are perhaps sensitive to different populations of AGN (blazars and radio galaxies vs. Seyfert galaxies).

3.3. Identification of near-infrared counterparts

It is well known that the AGN are prominent in the near-infrared band, and their variability can be used to identify them (e.g. Edelson et al. 1987).

These two considerations prompted us to cross-identify our objects with the point source catalogue of the VISTA (Visual and Infrared Survey Telescope for Astronomy; Emerson et al. 2006) Survey of the MC system (VMC; Cioni et al. 2011). VMC is an ESO public survey, carried out with the wide-field near-infrared camera VIRCAM (VISTA InfraRed CAMera; Dalton et al. 2006), mounted at the European Southern Observatory’s (ESO) VISTA 4.1 m telescope. More information about the telescope, the data flow system and the archive access to the data is given in Irwin et al. (2004); Emerson et al. (2004, 2006); González-Fernández et al. (2018); Cross et al. (2012) and Cioni et al. (2011) provides a detailed description of the VMC’s observing strategy. In short, the VMC covers 170 deg² around the MCs, Bridge and Stream, down to $K_s=20.3$ mag ($S/N \sim 10$; Vega system) in three epochs in the Y and J , and in 12 epochs (each of which consists of two or more individual pawprint observations) in the K_s band, spread over a year or longer.

At first we searched for the closest matches within 3'' for our 276 sources with the VMC obtained until March 2017 and identified 274 matches. To evaluate the probability for random coincidence we repeated the search after moving the source coordinates 3' to the east, and found 191 matches – these constitute a reference sample. The colour–colour diagram of the infrared counterparts with detections in all three bands is shown in Fig. 7. The inset shows histograms of the angular separation for the closest match for both the main and reference samples. Note that in many cases, there is more than one counterpart within 3''; those were not counted in the histogram for the main sample, and the higher counts in the reference histogram at separations $\geq 1''$ reflect the existence of additional VMC sources near the position of the objects in our sample. Apparently, the cross-identifications with separations $\leq 0''.5$ are secure, and the random coincidences dominate the larger separations. Therefore, we adopt $0''.5$ as a final matching radius for the VMC cross correlations and the subsequent analysis. This limit guarantees virtually zero contamination, as can be seen from the separation histogram (Fig. 7, inset panel). Another conclusion we draw from this diagram is that the reference sample consists mostly of stars, which is clear from the similarity of the locus it occupies with the stellar locus in Fig. 2 from Cioni et al. (2013). The location of the counterparts strongly supports the AGN nature.

Next, we extracted from the VMC catalogue the light curves for all the identified counterparts. For each light curve we calculated a linear fit of the K_s magnitude versus time – this is a simple parametrisation of the objects’ variability, following Cioni et al. (2013) and Ivanov et al. (2016). The properties of the light curves of the target and reference samples are summarised in Fig. 8. Clearly, the identified counterparts are more variable than a randomly selected sample, as expected for a sample dominated by AGN – in good agreement with the results of Cioni et al. (2013) and Ivanov et al. (2016). Note that the difference in the slopes is more evident if we only consider objects observed with at least 15 epochs. Our experiments with the slopes indicated that a smaller number of observations produces less than reliable slopes.

The counterparts of our sample tend to be brighter than the counterparts of the reference sample. The latter conclusion accounts, at least partially, for the larger number of epochs of the counterparts to “real” objects than for the counterparts to the

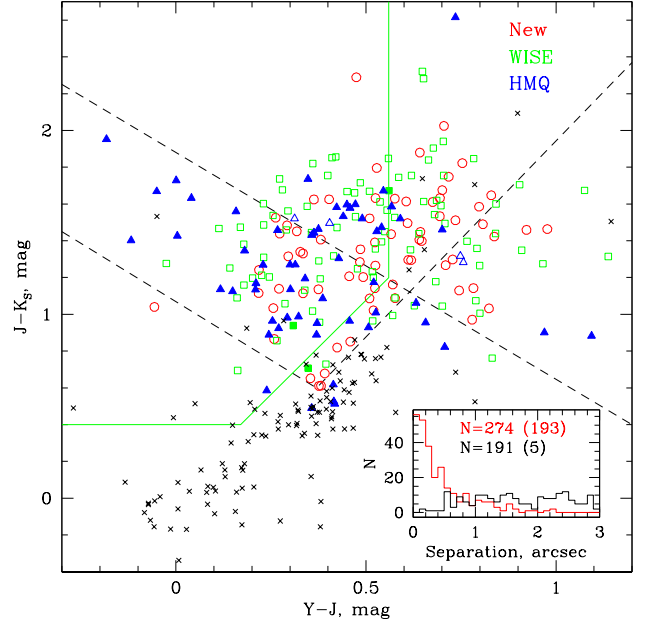


Fig. 7: VMC colour–colour diagram. The lines follow Cioni et al. (2013) and show regions where known quasars (upper left of the dashed black lines) and planetary nebulae (left of the green wedge) were found. Our objects are marked with red circles if they are newly identified, green squares if they were identified in the WISE data, or blue triangles if they were present in the HMQ/MILLIQUAS. The symbols are open if there has been no spectroscopic follow up, and solid if the objects have known redshifts from spectra. The reference sample is plotted with black crosses. The inset shows histograms of the angular separations between the objects and their counterparts for our sample (red) and for the reference sample (black).

“random” objects. Finally, we note that no constraint was imposed on whether the VMC matches are point-like or extended. This was motivated by the fact that some of the confirmed low redshift quasars in Ivanov et al. (2016) were classified as extended, e.g. the VMC has enough spatial resolution to see the host. Furthermore, background quasars can be contaminated by imperfectly aligned foreground VMC stars, giving the quasars an extended appearance.

3.4. Multi-wavelength properties

To investigate the distribution of the sources in the mid-infrared (ALLWISE) and near-infrared (VISTA) parameter space as a function of the total X-ray flux (0.2–12 keV) and the infrared (ALLWISE and VISTA) magnitudes, we plotted colour–colour diagram in Figs. 9 and 10. We found that the sample is homogeneously distributed within the ALLWISE ($x \equiv \log \frac{(f_{12\mu m})}{(f_{4.6\mu m})}$) versus $y \equiv \log \frac{(f_{4.6\mu m})}{(f_{3.4\mu m})}$) and VISTA ($Y-J$ and $J-K$) colour–colour space as a function of their X-ray fluxes and the ALLWISE and VISTA magnitudes. The median of the ALLWISE magnitudes are 15.79, 14.88 and 11.88 mag in the W1, W2 and W3 bands and the corresponding standard deviations are 1.06, 1.00 and 0.92 mag respectively. The corresponding median values of the VISTA magnitudes in the Y , J and K_s bands are 19.00, 18.58

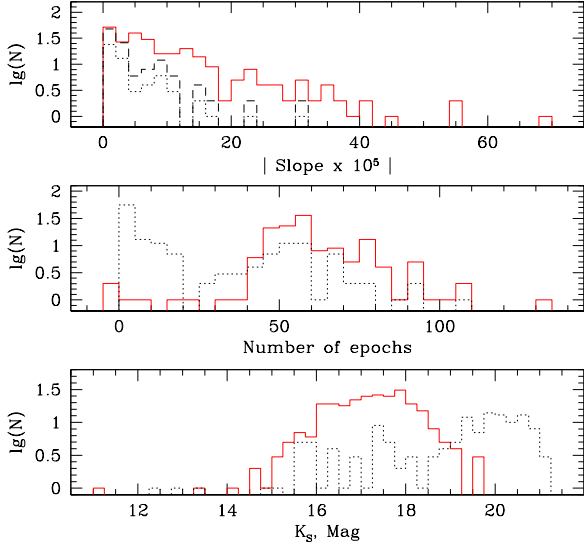


Fig. 8: Properties of the VMC K_S band light curves for the counterparts to our targets (red solid line) and of the light curves for the counterparts to the reference sample (black dotted line). The top panel shows histograms of the linear fits' slopes for objects with 15 or more epochs, so only reliable slopes are considered in the comparison. The black dashed line is the same as the black dotted, but scaled to match the level of the first bin. The middle panel shows histograms of the number of available K_S epochs, and the bottom panel the K_S band apparent luminosity functions averaged over epochs.

and 17.27 mag with standard deviations of 1.03, 1.1 and 1.06 mag respectively.

A positive correlation is observed between the integrated X-ray flux (0.2–12 keV) and the ALLWISE and VISTA magnitudes. From Fig. 11 it can be seen that the brightest objects in X-rays correspond to the brightest objects in the W1, W2 and W3 bands of the ALLWISE data, and the Y , J , and K_s magnitudes in the VISTA data.

3.5. Identification of new candidates

We identified 81 new AGN candidates from a sample that was selected using the ALLWISE mid-infrared selection criteria of Mateos et al. (2012) albeit with a lower S/N of 3, but with a corresponding X-ray association. This sample is not included in any of the large all-sky AGN catalogues of Secrest et al. (2015) and Flesch (2015, 2017). To ensure that they have not been reported previously, we searched within $3''$ of all the source positions in the VizieR database³. We found that for 31 of the 81 sources, the corresponding ALLWISE counterparts were identified in the ARCHES (Astronomical Resource Cross-matching for High Energy Studies) database (Motch et al. 2016) although source classification was not performed. 22 of the 31 were however included in Kozłowski & Kochanek (2009) as AGN candidates. This makes 59 new sources catalogued as AGN candidates for the first time. The X-ray, mid-infrared and near-infrared colours of the sources, as well as the variability in the near-infrared band strongly support their AGN nature and the level

of contamination is likely to be almost negligible. The new candidates therefore make a very promising subset for optical spectroscopic follow-up and are listed in Table A.1.

3.6. Optical spectroscopy of new candidates

In order to verify the robustness of our selection of new candidates, we performed optical spectroscopic follow-up of 6 randomly chosen objects out of the 15 brightest (in X-rays) candidates listed in Table A.1. Low-resolution ($R=\lambda/\Delta\lambda\sim 440$) spectra over $\lambda 4450\text{--}8650\text{\AA}$ were obtained with the FOcal Reducer and low dispersion Spectrograph (FORS2; Appenzeller et al. 1998) at the ESO Very Large Telescope. The set up was: long-slit mode, grism 300V+10, order sorting filter GG435+81, slit width $1.3''$. Further details are listed in Table A.2. The data reduction closely followed Ivanov et al. (2016), except a newer Reflex-based (Freudling et al. 2013) ESO pipeline version (5.3.23) was used. The finding charts are shown in Fig. B.1, the final spectra are shown in Fig. 12, and the measured emission lines are listed in Table A.3. The candidates are presented in decreasing order of their X-ray fluxes. The results confirm that all of the 6 objects that were followed up are AGN. One of them (candidate 59) is a distant quasar with $z = 2.23$. The presence of a broad MgII line in candidates 18, 26 and 35 also confirms that they are quasars. Candidates 06 and 47 are Seyfert galaxies, and the presence of narrow emission lines indicate type 2 Seyferts. Although the 100% success rate of our initial follow-up of the 6 candidates does not guarantee the validity of all the other candidates, the results are in further support of the robustness of our selection and strongly encourage future follow-ups.

3.7. Comparison of the sample with the expected population of AGN

Seventy-one percent of the X-ray point sources detected in the SMC region by the *XMM-Newton* are expected to be AGN behind the SMC (Sturm et al. 2013b). This implies that ~ 3158 of the 4311 detected unique sources are AGN. Our identification of 276 sources constitute only a small fraction of the entire expected population. This can be attributed to the limitations of the selection criterion used in this work as well as the data sets which were used for the identification of the sample.

The AGN selection wedge is defined using the Bright Ultra-hard *XMM-Newton* survey (BUXS). This is one of the largest complete flux-limited samples of bright (flux between $4.5\text{--}10\text{ keV} > 6.0 \times 10^{-14}\text{ erg cm}^{-2}\text{ s}^{-1}$) and ultra-hard ($4.5\text{--}10\text{ keV}$) X-ray selected AGN. The sample selected in this work is heavily biased towards these properties which is evident by the fact that the median flux of the sample is very close to the BUXS value. Mateos et al. (2012) further noted that the selection completeness was significantly smaller for type 2 AGN at X-ray luminosities ($2\text{--}10\text{ keV} < 10^{44}\text{ erg s}^{-1}$) than type 1 AGN. This is mainly attributed to different luminosity distributions for the two classes of AGN, with type 2 being intrinsically less luminous. Further a sharp decrease in the X-ray detection fraction of ALLWISE objects is expected at $\log \left(\frac{f_{12\mu\text{m}}}{f_{4.6\mu\text{m}}} \right) \gtrsim 0.7 - 0.8$. This is also seen in our sample (Fig. 13), when comparing the AGN identified using the ALLWISE criterion in this work with the entire sample of ALLWISE sources located within the area of the *XMM-Newton* survey which fulfilled the criterion of Mateos et al. (2012).

In order to illustrate the limitations of the data sets which were used for the identification of the sample, we correlated the sample of AGN candidates from Sturm et al. (2013b) which

³ <http://vizier.u-strasbg.fr/>

were not confirmed in this work, with the ALLWISE catalogue (using sources with $S/N \geq 3$ in W1, W2 and W3 bands & `cc_flags == '0000'`). Out of 1989 sources only 134 were found to have a secure ALLWISE counterpart (shown in Fig. 13). The small fraction of the AGN candidates identified with an ALLWISE counterpart is consistent with the fact that only 276 AGN were identified when correlating the entire unique source list of the *XMM-Newton* SMC survey with the ALLWISE catalogue. The most intriguing point is that almost all of these sources overlap with the horizontal sequence of normal galaxies in the ALLWISE colour–colour space. This points to the fact that most of these 134 sources being at the faint end of the X-ray flux (near the detection limit of the *XMM-Newton* survey) may have contribution from the host galaxy in the mid-infrared emission, so that they fall outside the selection wedge and overlap with normal galaxies (Mateos et al. 2012; Mountrichas et al. 2017, and references therein). This is further ascertained in Fig. 11, which shows the new AGN candidates which are identified in this work by relaxing the S/N threshold in the W1, W2 and W3 bands. It is evident from the figure that these sources tend to be intrinsically less luminous, and they lie near the detection thresholds in both the X-ray and infrared bands. As the correlation between the X-ray and infrared bands has a relatively large spread, it is possible that many of these sources fall below the detection threshold in the ALLWISE bands even though they are detected in the X-ray band. This is supported by the very small fraction of ALLWISE counterparts identified as AGN candidates from Sturm et al. (2013b). We further searched for the ALLWISE counterparts of the 58 sources exclusively selected from the HMQ and MILLIQUAS catalogue using the same criteria as above. Only 10 sources were found to have a secure ALLWISE counterpart, plotted in Fig. 13. As in the case of AGN candidates from Sturm et al. (2013b), all of these sources lie in the horizontal sequence of normal galaxies in the ALLWISE colour–colour space. This is in further support of the fact that not all AGN lie within the ALLWISE selection wedge of Mateos et al. (2012).

4. Summary & Conclusions

In this paper we present a catalogue of 276 AGN behind the SMC by correlating an updated X-ray point source catalogue of the *XMM-Newton* SMC survey with already known AGN from the literature or selected using ALLWISE mid-infrared colour criteria. Ninety sources in the sample have confirmed redshifts, and the redshift distribution indicates that we detect sources from nearby Seyfert galaxies to distant quasars. We investigated the X-ray luminosity distribution (not corrected for absorption) of the sources and compared it with the infrared luminosity distribution (both in the rest-frame).

We identified near-infrared counterparts of the sources from the VISTA observations, and confirmed that the VISTA colours and variability are compatible with that expected from AGN. We also confirm that the X-ray hardness ratios are compatible with that expected typically for AGN. These two results validate the robustness of our selection. We found the sources to be homogeneously distributed in the ALLWISE and VISTA colour–colour space where the AGN are expected to be located. A positive correlation was observed between the integrated X-ray flux (0.2–12 keV) and the ALLWISE and VISTA magnitudes.

The sample contains 81 newly identified candidates (with 59 being introduced for the first time as AGN candidates) which were selected using the ALLWISE mid-infrared colours but with a lower S/N criterion than used by Secrest et al. (2015). An ini-

tial optical spectroscopic follow-up of 6 out of the 81 candidates confirmed that all six are AGN. This strongly supports the robustness of the sample of candidate AGN and encourages further follow-up of the rest of the sample. We also identified possible candidates for distant obscured quasars behind the SMC. All of these make a very promising subset for optical spectroscopic follow-up to confirm the nature of the sources, and/or X-ray spectral analysis to determine the degree and nature of obscuration towards the source.

In this work $\sim 75\%$ of the sources are identified using mid-infrared colour selection criteria. This technique is very useful in finding the most luminous and obscured AGN. However, the sample is expected to be incomplete at lower luminosities where the

References

- Appenzeller, I., Fricke, K., Fürtig, W., et al. 1998, *The Messenger*, 94, 1
 Assef, R. J., Stern, D., Kochanek, C. S., et al. 2013, *ApJ*, 772, 26
 Brightman, M. & Nandra, K. 2012, *MNRAS*, 422, 1166
 Caputi, K. I. 2014, *International Journal of Modern Physics D*, 23, 1430015
 Cioni, M.-R. L., Clementini, G., Girardi, L., et al. 2011, *A&A*, 527, A116
 Cioni, M.-R. L., Girardi, L., Moretti, M. L., et al. 2014, *A&A*, 562, A32
 Cioni, M.-R. L., Kamath, D., Rubele, S., et al. 2013, *A&A*, 549, A29
 Cross, N. J. G., Collins, R. S., Mann, R. G., et al. 2012, *A&A*, 548, A119
 Dalton, G. B., Caldwell, M., Ward, A. K., et al. 2006, in *Proc. SPIE*, Vol. 6269, Society of Photo-Optical Instrumentation Engineers (SPIE) Conference Series, 62690X
 Della Ceca, R., Caccianiga, A., Severgnini, P., et al. 2008, *A&A*, 487, 119
 Dickey, J. M. & Lockman, F. J. 1990, *ARA&A*, 28, 215
 Dobrzycki, A., Macri, L. M., Stanek, K. Z., & Groot, P. J. 2003a, *AJ*, 125, 1330
 Dobrzycki, A., Stanek, K. Z., Macri, L. M., & Groot, P. J. 2003b, *AJ*, 126, 734
 Donley, J. L., Koekemoer, A. M., Brusa, M., et al. 2012, *ApJ*, 748, 142
 Edelson, R. A., Malkan, M. A., & Rieke, G. H. 1987, *ApJ*, 321, 233
 Emerson, J., McPherson, A., & Sutherland, W. 2006, *The Messenger*, 126, 41
 Emerson, J. P., Irwin, M. J., Lewis, J., et al. 2004, in *Proc. SPIE*, Vol. 5493, *Optimizing Scientific Return for Astronomy through Information Technologies*, ed. P. J. Quinn & A. Bridger, 401–410
 Eyer, L. 2002, *Acta Astron.*, 52, 241
 Fabian, A. C. & Iwasawa, K. 1999, *MNRAS*, 303, L34
 Fiore, F., Puccetti, S., Brusa, M., et al. 2009, *ApJ*, 693, 447
 Flesch, E. W. 2015, *PASA*, 32, e010
 Flesch, E. W. 2017, *VizieR Online Data Catalog*, 7277
 Freudling, W., Romaniello, M., Bramich, D. M., et al. 2013, *A&A*, 559, A96
 Gandhi, P., Horst, H., Smette, A., et al. 2009, *A&A*, 502, 457
 Geha, M., Alcock, C., Allsman, R. A., et al. 2003, *AJ*, 125, 1
 Gilli, R., Comastri, A., & Hasinger, G. 2007, *A&A*, 463, 79
 González-Fernández, C., Hodgkin, S. T., Irwin, M. J., et al. 2018, *MNRAS*, 474, 5459
 Haberl, F., Sturm, R., Ballet, J., et al. 2012, *A&A*, 545, A128
 Hasinger, G., Altieri, B., Arnaud, M., et al. 2001, *A&A*, 365, L45
 Hasinger, G., Cappelluti, N., Brunner, H., et al. 2007, *ApJS*, 172, 29
 Irwin, M. J., Lewis, J., Hodgkin, S., et al. 2004, in *Proc. SPIE*, Vol. 5493, *Optimizing Scientific Return for Astronomy through Information Technologies*, ed. P. J. Quinn & A. Bridger, 411–422
 Ivanov, V. D., Cioni, M.-R. L., Bekki, K., et al. 2016, *A&A*, 588, A93
 Jansen, F., Lumb, D., Altieri, B., et al. 2001, *A&A*, 365, L1
 Kallivayalil, N., van der Marel, R. P., Besla, G., Anderson, J., & Alcock, C. 2013, *ApJ*, 764, 161
 Kelly, B. C., Bechtold, J., & Siemiginowska, A. 2009, *ApJ*, 698, 895
 Kozłowski, S. & Kochanek, C. S. 2009, *ApJ*, 701, 508
 Kozłowski, S., Kochanek, C. S., & Udalski, A. 2011, *ApJS*, 194, 22
 Kozłowski, S., Onken, C. A., Kochanek, C. S., et al. 2013, *ApJ*, 775, 92
 Lacy, M., Storrie-Lombardi, L. J., Sajina, A., et al. 2004, *ApJS*, 154, 166
 Lanzuisi, G., Piconcelli, E., Fiore, F., et al. 2009, *A&A*, 498, 67
 Mateos, S., Alonso-Herrero, A., Carrera, F. J., et al. 2012, *MNRAS*, 426, 3271
 Mills, B. Y., Little, A. G., Durdin, J. M., & Kesteven, M. J. 1982, *MNRAS*, 200, 1007
 Motch, C., Carrera, F., Genova, F., et al. 2016, *ArXiv e-prints*
 Mountrichas, G., Georgantopoulos, I., Secrest, N. J., et al. 2017, *MNRAS*, 468, 3042
 Rosen, S. R., Webb, N. A., Watson, M. G., et al. 2016, *A&A*, 590, A1
 Rovilos, E., Georgantopoulos, I., Akylas, A., et al. 2014, *MNRAS*, 438, 494
 Secrest, N. J., Dudik, R. P., Dorland, B. N., et al. 2015, *ApJS*, 221, 12

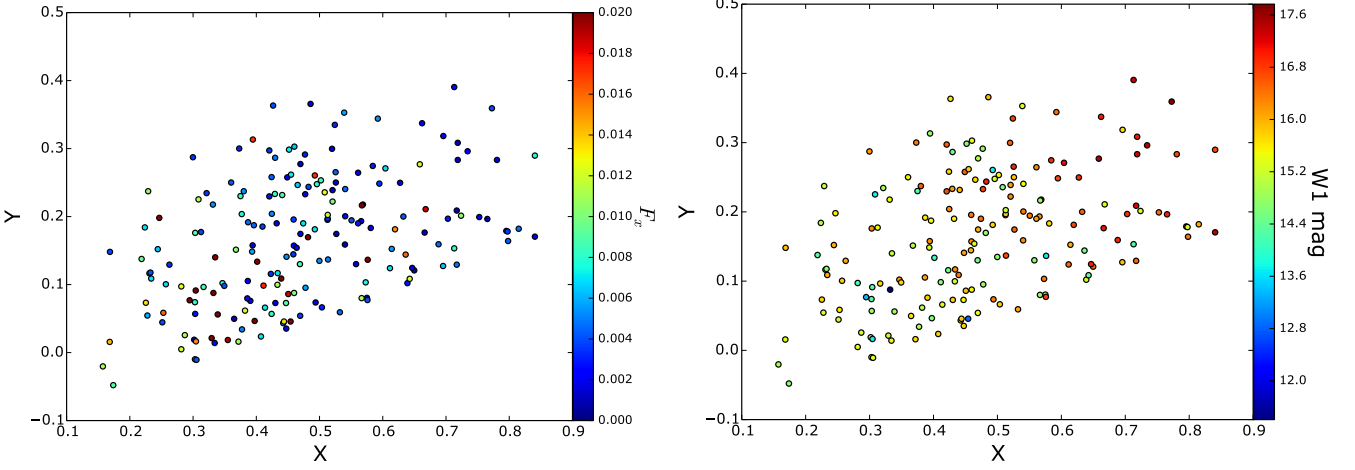


Fig. 9: Distribution of the sample in the ALLWISE two-colour selection plane (Mateos et al. 2012). $x \equiv \log \left(\frac{f_{12\mu m}}{f_{4.6\mu m}} \right)$ and $y \equiv \log \left(\frac{f_{4.6\mu m}}{f_{3.4\mu m}} \right)$. X-ray flux (F_x) is in units of $10^{-11} \text{ erg cm}^{-2} \text{ s}^{-1}$ in the energy range of 0.2–12 keV. The two figures are representative of the distribution of the sample in the ALLWISE plane, and the variation with W2 and W3 magnitudes show a similar pattern.

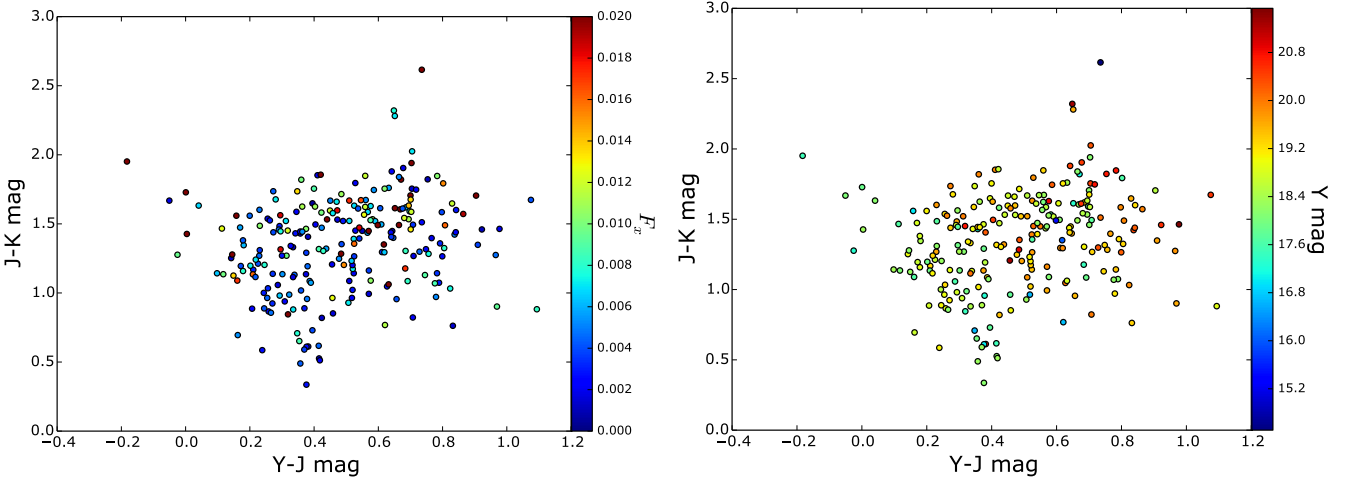


Fig. 10: Distribution of the sample in the VISTA two-colour selection plane (Cioni et al. 2013). The two figures are representative of the distribution of the sample in the VISTA plane, and the variation with J and K_s magnitudes show a similar pattern. X-ray flux (F_x) as in Fig. 9.

- Severgnini, P., Caccianiga, A., & Della Ceca, R. 2012, *A&A*, 542, A46
 Stanimirovic, S., Staveley-Smith, L., Dickey, J. M., Sault, R. J., & Snowden, S. L. 1999, *MNRAS*, 302, 417
 Stern, D. 2015, *ApJ*, 807, 129
 Stern, D., Assef, R. J., Benford, D. J., et al. 2012, *ApJ*, 753, 30
 Stern, D., Eisenhardt, P., Gorjian, V., et al. 2005, *ApJ*, 631, 163
 Sturm, R., Drašković, D., Filipović, M. D., et al. 2013a, *A&A*, 558, A101
 Sturm, R., Haberl, F., Pietsch, W., et al. 2013b, *A&A*, 558, A3
 Terashima, Y., Hirata, Y., Awaki, H., et al. 2015, *ApJ*, 814, 11
 Tinney, C. G., Da Costa, G. S., & Zinnecker, H. 1997, *MNRAS*, 285, 111
 Tozzi, P., Gilli, R., Mainieri, V., et al. 2006, *A&A*, 451, 457
 Vanden Berk, D. E., Richards, G. T., Bauer, A., et al. 2001, *AJ*, 122, 549
 Wilkes, B. J., Wright, A. E., Jauncey, D. L., & Peterson, B. A. 1983, *Proceedings of the Astronomical Society of Australia*, 5, 2
 Wright, E. L., Eisenhardt, P. R. M., Mainzer, A. K., et al. 2010, *AJ*, 140, 1868

contamination from the host galaxy begins to dominate and renders the mid-infrared colours bluer so that they fall outside the selection wedge (Mateos et al. 2012; Mountrichas et al. 2017, and references therein). Therefore, we possibly miss the faint AGN using these criteria which become indistinguishable in X-rays from star-forming galaxies.

Acknowledgements. The *XMM-Newton* project is supported by the Bundesministerium für Wirtschaft und Technologie/Deutsches Zentrum für Luft- und Raumfahrt (BMWi/DLR, FKZ 50 OX 0001) and the Max-Planck Society. M.-R.L.C. has received support from the European Research Council (ERC) under European Unions Horizon 2020 research and innovation programme (grant agreement No 682115). We thank the Cambridge Astronomy Survey Unit (CASU) and the Wide Field Astronomy Unit (WFAU) in Edinburgh for providing calibrated data products under the support of the Science and Technology Facility Council (STFC).

References

- Appenzeller, I., Fricke, K., Fürtig, W., et al. 1998, *The Messenger*, 94, 1
 Assef, R. J., Stern, D., Kochanek, C. S., et al. 2013, *ApJ*, 772, 26
 Brightman, M. & Nandra, K. 2012, *MNRAS*, 422, 1166
 Caputi, K. I. 2014, *International Journal of Modern Physics D*, 23, 1430015
 Cioni, M.-R. L., Clementini, G., Girardi, L., et al. 2011, *A&A*, 527, A116
 Cioni, M.-R. L., Girardi, L., Moretti, M. I., et al. 2014, *A&A*, 562, A32
 Cioni, M.-R. L., Kamath, D., Rubele, S., et al. 2013, *A&A*, 549, A29
 Cross, N. J. G., Collins, R. S., Mann, R. G., et al. 2012, *A&A*, 548, A119
 Dalton, G. B., Caldwell, M., Ward, A. K., et al. 2006, in *Proc. SPIE*, Vol. 6269, Society of Photo-Optical Instrumentation Engineers (SPIE) Conference

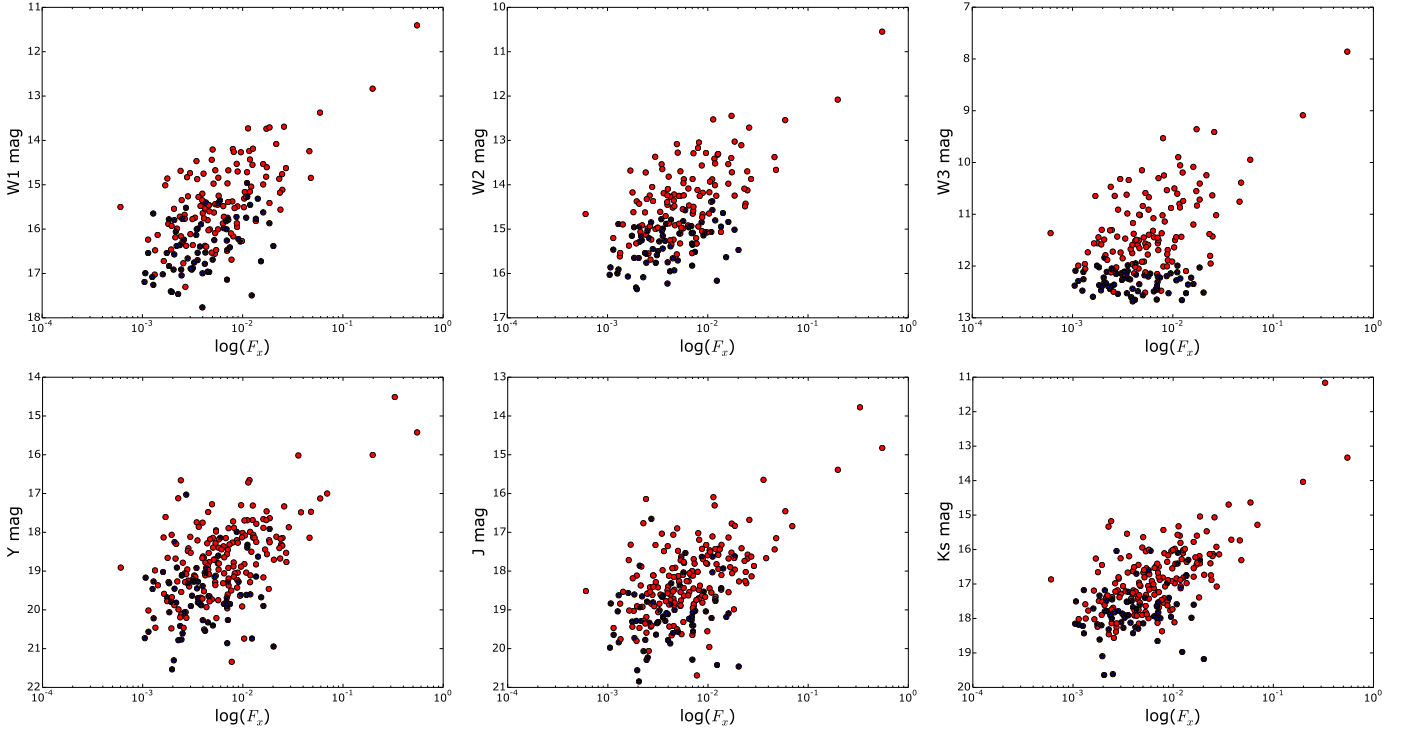


Fig. 11: Relation between the X-ray flux and the ALLWISE and VISTA magnitudes. X-ray flux (F_x) as in Fig. 9. Blue dots mark the new candidates identified in this work.

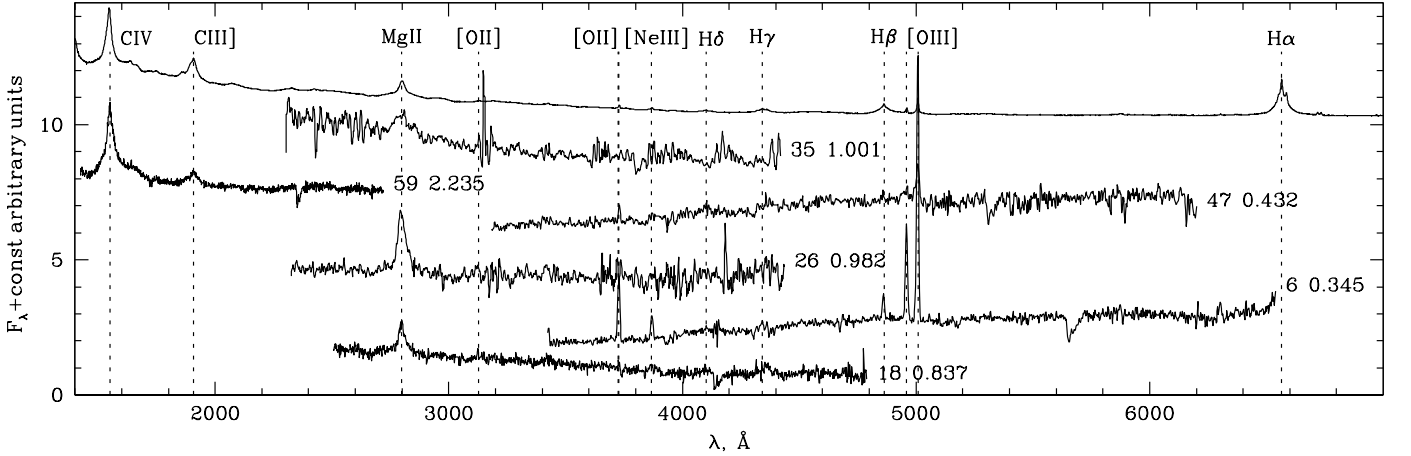


Fig. 12: Spectra of the AGN candidates shifted to rest-frame wavelength. The spectra were smoothed, normalised to an average value of one and offset vertically for display purposes. The SDSS composite quasar spectrum (Vanden Berk et al. 2001) is shown at the top.

Series, 62690X
 Della Ceca, R., Caccianiga, A., Severgnini, P., et al. 2008, *A&A*, 487, 119
 Dickey, J. M. & Lockman, F. J. 1990, *ARA&A*, 28, 215
 Dobrzycki, A., Macri, L. M., Stanek, K. Z., & Groot, P. J. 2003a, *AJ*, 125, 1330
 Dobrzycki, A., Stanek, K. Z., Macri, L. M., & Groot, P. J. 2003b, *AJ*, 126, 734
 Donley, J. L., Koekemoer, A. M., Brusa, M., et al. 2012, *ApJ*, 748, 142
 Edelson, R. A., Malkan, M. A., & Rieke, G. H. 1987, *ApJ*, 321, 233
 Emerson, J., McPherson, A., & Sutherland, W. 2006, *The Messenger*, 126, 41
 Emerson, J. P., Irwin, M. J., Lewis, J., et al. 2004, in *Proc. SPIE*, Vol. 5493, *Optimizing Scientific Return for Astronomy through Information Technologies*, ed. P. J. Quinn & A. Bridger, 401–410
 Eyer, L. 2002, *Acta Astron.*, 52, 241
 Fabian, A. C. & Iwasawa, K. 1999, *MNRAS*, 303, L34
 Fiore, F., Puccetti, S., Brusa, M., et al. 2009, *ApJ*, 693, 447
 Flesch, E. W. 2015, *PASA*, 32, e010
 Flesch, E. W. 2017, *VizieR Online Data Catalog*, 7277

Freudling, W., Romaniello, M., Bramich, D. M., et al. 2013, *A&A*, 559, A96
 Gandhi, P., Horst, H., Smette, A., et al. 2009, *A&A*, 502, 457
 Geha, M., Alcock, C., Allsman, R. A., et al. 2003, *AJ*, 125, 1
 Gilli, R., Comastri, A., & Hasinger, G. 2007, *A&A*, 463, 79
 González-Fernández, C., Hodgkin, S. T., Irwin, M. J., et al. 2018, *MNRAS*, 474, 5459
 Haberl, F., Sturm, R., Ballet, J., et al. 2012, *A&A*, 545, A128
 Hasinger, G., Altieri, B., Arnaud, M., et al. 2001, *A&A*, 365, L45
 Hasinger, G., Cappelluti, N., Brunner, H., et al. 2007, *ApJS*, 172, 29
 Irwin, M. J., Lewis, J., Hodgkin, S., et al. 2004, in *Proc. SPIE*, Vol. 5493, *Optimizing Scientific Return for Astronomy through Information Technologies*, ed. P. J. Quinn & A. Bridger, 411–422
 Ivanov, V. D., Cioni, M.-R. L., Bekki, K., et al. 2016, *A&A*, 588, A93
 Jansen, F., Lumb, D., Altieri, B., et al. 2001, *A&A*, 365, L1
 Kallivayalil, N., van der Marel, R. P., Besla, G., Anderson, J., & Alcock, C. 2013, *ApJ*, 764, 161

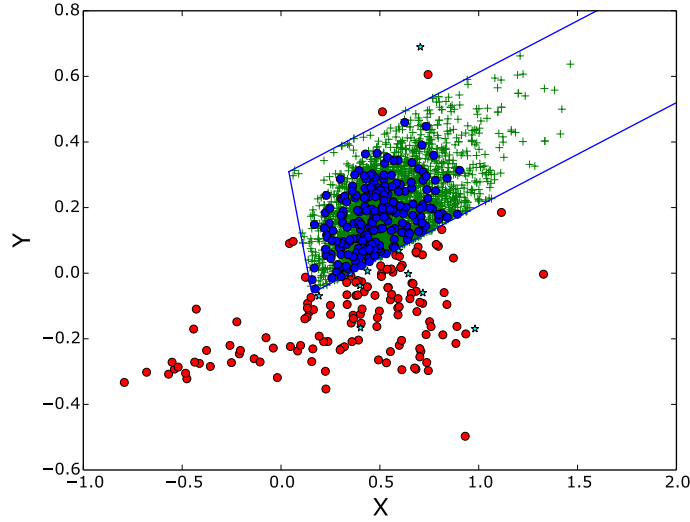


Fig. 13: Distribution of sources in the ALLWISE two-colour selection plane (Mateos et al. 2012). $x \equiv \log \frac{(f_{12\mu m})}{(f_{4.6\mu m})}$ and $y \equiv \log \frac{(f_{4.6\mu m})}{(f_{3.4\mu m})}$. Blue circles mark the 218 AGN identified using the ALLWISE criteria. Green crosses indicate all ALLWISE sources located within the *XMM-Newton* survey area which fulfilled the criterion of Mateos et al. (2012). Red circles are AGN candidates from Sturm et al. (2013b) which were found to have an ALLWISE counterpart. Cyan stars are HMQ/MILLIQUAS sources which were found to have an ALLWISE counterpart.

- Kelly, B. C., Bechtold, J., & Siemiginowska, A. 2009, *ApJ*, 698, 895
Kozłowski, S. & Kochanek, C. S. 2009, *ApJ*, 701, 508
Kozłowski, S., Kochanek, C. S., & Udalski, A. 2011, *ApJS*, 194, 22
Kozłowski, S., Onken, C. A., Kochanek, C. S., et al. 2013, *ApJ*, 775, 92
Lacy, M., Storrie-Lombardi, L. J., Sajina, A., et al. 2004, *ApJS*, 154, 166
Lanzuisi, G., Piconcelli, E., Fiore, F., et al. 2009, *A&A*, 498, 67
Mateos, S., Alonso-Herrero, A., Carrera, F. J., et al. 2012, *MNRAS*, 426, 3271
Mills, B. Y., Little, A. G., Durdin, J. M., & Kesteven, M. J. 1982, *MNRAS*, 200, 1007
Motch, C., Carrera, F., Genova, F., et al. 2016, *ArXiv e-prints*
Mountrichas, G., Georgantopoulos, I., Secrest, N. J., et al. 2017, *MNRAS*, 468, 3042
Rosen, S. R., Webb, N. A., Watson, M. G., et al. 2016, *A&A*, 590, A1
Rovilos, E., Georgantopoulos, I., Akylas, A., et al. 2014, *MNRAS*, 438, 494
Secrest, N. J., Dudik, R. P., Dorland, B. N., et al. 2015, *ApJS*, 221, 12
Severgnini, P., Caccianiga, A., & Della Ceca, R. 2012, *A&A*, 542, A46
Stanimirovic, S., Staveley-Smith, L., Dickey, J. M., Sault, R. J., & Snowden, S. L. 1999, *MNRAS*, 302, 417
Stern, D. 2015, *ApJ*, 807, 129
Stern, D., Assef, R. J., Benford, D. J., et al. 2012, *ApJ*, 753, 30
Stern, D., Eisenhardt, P., Gorjian, V., et al. 2005, *ApJ*, 631, 163
Sturm, R., Drašković, D., Filipović, M. D., et al. 2013a, *A&A*, 558, A101
Sturm, R., Haberl, F., Pietsch, W., et al. 2013b, *A&A*, 558, A3
Terashima, Y., Hirata, Y., Awaki, H., et al. 2015, *ApJ*, 814, 11
Tinney, C. G., Da Costa, G. S., & Zinnecker, H. 1997, *MNRAS*, 285, 111
Tozzi, P., Gilli, R., Mainieri, V., et al. 2006, *A&A*, 451, 457
Vanden Berk, D. E., Richards, G. T., Bauer, A., et al. 2001, *AJ*, 122, 549
Wilkes, B. J., Wright, A. E., Jauncey, D. L., & Peterson, B. A. 1983, *Proceedings of the Astronomical Society of Australia*, 5, 2
Wright, E. L., Eisenhardt, P. R. M., Mainzer, A. K., et al. 2010, *AJ*, 140, 1868

Appendix A: Tables

Table A.1: Newly identified AGN candidates from the *XMM-Newton* SMC survey selected using ALLWISE mid-infrared colour selection.

Candidate	Designation	R.A.	Dec.	Error ($l_{12\mu m}$) ($l_{4.6\mu m}$)	X $\log \left(\frac{f_{4.6\mu m}}{f_{12\mu m}} \right)$	Y $\times 10^{-11} \text{ erg cm}^{-2} \text{ s}^{-1}$	F_x (0.2–12 keV) $\text{erg cm}^{-2} \text{ s}^{-1}$	eF _x mag	Y – J mag	J – K _s	XMM_id
1	J002523.92–712322.4	6.3497	–71.3896	0.1059	0.244	0.152	0.0065	0.0010	0.619	1.290	–
2	J002606.42–711301.6	6.5267	–71.2171	0.1505	0.633	0.200	0.0042	0.0007	0.217	1.120	–
3	J002636.61–712409.5	6.6525	–71.4027	0.1365	0.513	0.195	0.0022	0.0002	0.258	0.866	–
4	J002638.65–712104.2	6.7444	–71.3512	0.2273	0.604	0.271	0.0070	0.0004	0.576	1.630	–
5	J003816.75–725101.0	9.5698	–72.8503	0.1011	0.430	0.073	0.0018	0.0004	0.710	1.270	J003815.9–725058
6	J003918.19–730331.5	9.8258	–73.0588	0.0880	0.168	0.016	0.0140	0.0020	0.695	1.630	J003917.7–730330
7	J004140.61–735156.8	10.4192	–73.8658	0.0867	0.305	–0.011	0.0043	0.0009	0.606	1.610	–
8	J004551.17–734018.6	11.4632	–73.6719	0.0886	0.303	–0.009	0.0050	0.0004	0.566	1.440	J004551.3–734017
9	J004613.07–722539.5	11.5545	–72.4276	0.1894	0.619	0.181	0.0150	0.0020	0.493	1.200	J004612.9–722535
10	J004633.42–734443.2	11.6393	–73.7453	0.1022	0.334	0.014	0.0027	0.0005	0.376	0.611	J004632.9–734444
11	J004825.64–720032.6	12.1069	–72.0091	0.2030	0.520	0.285	0.0044	0.0006	0.000	1.790	J004825.8–720032
12	J004914.34–744537.6	12.3098	–74.7605	0.0849	0.317	0.096	0.0087	0.0010	0.354	0.652	–
13	J004929.63–721051.5	12.3735	–72.1810	0.1274	0.425	0.204	0.0052	0.0005	0.780	0.971	J004929.6–721050
14	J004938.79–715052.5	12.4116	–71.8479	0.2460	0.717	0.209	0.0010	0.0002	0.754	1.820	J004938.4–715052
15	J005015.69–743801.6	12.5654	–74.6338	0.0978	0.300	0.287	0.0034	0.0004	0.271	1.140	J005015.4–743802
16	J005019.50–714817.2	12.5813	–71.8048	0.1070	0.387	0.105	0.0022	0.0005	0.528	1.800	J005019.0–714818
17	J005035.42–730815.7	12.6476	–73.1377	0.4217	0.717	0.140	0.0007	0.0001	0.0	0.0	J005035.6–730813
18	J005057.59–714132.1	12.7400	–71.6923	0.1348	0.573	0.103	0.0075	0.0010	0.824	1.030	J005057.3–714131
19	J005100.96–735011.9	12.7540	–73.8366	0.5307	0.903	0.314	0.0016	0.0005	0.0	2.360	J005101.2–735011
20	J005141.19–750049.6	12.9216	–75.0138	0.1727	0.584	0.274	0.0031	0.0005	0.292	1.480	J005141.0–750051
21	J005145.45–720911.1	12.9394	–72.1531	0.1997	0.559	0.299	0.0032	0.0003	–0.050	1.040	J005145.3–720910
22	J005153.04–715334.9	12.9710	–71.8930	0.2001	0.627	0.250	0.0020	0.0005	0.456	1.210	J005152.5–715340
23	J005202.89–720505.0	13.0121	–72.0847	0.3675	0.773	0.359	0.0040	0.0003	0.273	1.440	J005203.0–720505
24	J005240.23–745251.0	13.1677	–74.8809	0.1913	0.765	0.196	0.0011	0.0002	0.334	1.330	J005240.0–745252
25	J005301.41–713107.7	13.2559	–71.5188	0.1710	0.569	0.218	0.0018	0.0003	0.335	1.110	J005301.1–713105
26	J005326.06–714821.2	13.3586	–71.8059	0.0853	0.281	0.005	0.0120	0.0008	0.830	1.650	J005325.9–714821
27	J005410.60–705051.0	13.5442	–70.8475	0.2896	0.659	0.277	0.0120	0.0030	0.318	1.450	J005411.6–705052
28	J005415.32–743153.0	13.5638	–74.5314	0.1259	0.459	0.196	0.0037	0.0003	0.570	1.160	J005415.5–743153
29	J005456.84–720857.9	13.7368	–72.1494	0.1349	0.312	0.154	0.0062	0.0007	0	0	J005456.6–720856
30	J005540.46–720555.2	13.9186	–72.0987	0.1624	0.449	0.258	0.0021	0.0002	0.524	1.140	J005540.4–720555
31	J005611.06–703958.6	14.0461	–70.6663	0.3069	0.841	0.170	0.0020	0.0005	0.977	1.460	J005610.7–703957
32	J005622.87–743238.6	14.0953	–74.5441	0.1209	0.434	0.117	0.0070	0.0009	0.523	1.390	J005623.7–743236
33	J005652.51–721203.5	14.2188	–72.2010	0.2488	0.688	0.159	0.0046	0.0002	0.647	1.400	J005652.4–721203
34	J005652.57–712300.6	14.2191	–71.3835	0.1787	0.525	0.265	0.0045	0.0005	0.728	1.300	J005652.3–712300
35	J005749.75–711802.3	14.4573	–71.3006	0.0819	0.253	0.058	0.0160	0.0007	0.808	1.490	J005749.3–711801
36	J005811.52–714748.4	14.5480	–71.7968	0.1634	0.595	0.248	0.0036	0.0005	0.525	1.270	J005811.3–714748
37	J010004.54–711738.8	15.0190	–71.2941	0.1313	0.439	0.109	0.0200	0.0020	0.484	1.280	J010004.2–711737
38	J010033.38–715037.2	15.1391	–71.8437	0.1435	0.494	0.074	0.0024	0.0005	0.642	1.880	J010033.4–715039
39	J010035.78–714702.8	15.1491	–71.7841	0.2359	0.647	0.124	0.0016	0.0003	0.459	0.852	J010036.1–714700
40	J010053.72–711042.9	15.2289	–71.1786	0.1030	0.459	0.144	0.0036	0.0005	0.640	1.410	J010053.0–711042
41	J010109.33–723237.0	15.2889	–72.5436	0.0820	0.287	0.026	0.0110	0.0006	0.694	1.530	J010109.3–723237
42	J010140.41–722940.0	15.4184	–72.4945	0.1103	0.386	0.079	0.0028	0.0004	0.376	0.336	J010140.6–722941
43	J010155.58–722948.4	15.4816	–72.4968	0.0911	0.228	0.054	0.0059	0.0006	0.609	1.500	J010155.5–722948
44	J010231.92–730709.3	15.6330	–73.1193	0.1179	0.424	0.057	0.0081	0.0004	0.805	1.325	J010231.8–730708
45	J010252.62–721929.7	16.3568	–72.3249	0.1545	0.475	0.054	0.0031	0.0003	0.0	1.640	J010252.4–721927
46	J010630.55–723544.0	16.6273	–72.5956	0.1010	0.499	0.085	0.0021	0.0002	0.390	0.680	J010630.7–723546
47	J010849.53–721233.1	17.2064	–72.2092	0.0949	0.225	0.073	0.0140	0.0004	0.701	1.680	J010849.7–721233
48	J010927.41–723110.0	17.3642	–72.5195	0.1186	0.362	0.266	0.0050	0.0005	0.0	2.130	J010927.7–723109
49	J010934.35–720338.0	17.3931	–72.0606	0.1029	0.355	0.018	0.019	0.0006	0.864	1.571	J010934.5–720337
50	J011014.66–724228.6	17.5611	–72.7080	0.2437	0.719	0.283	0.0013	0.0003	0.381	1.410	J011014.3–724228
51	J011241.93–732830.6	18.1747	–73.4752	0.1766	0.513	0.137	0.0050	0.0005	0.837	1.420	J011242.2–732831
52	J011323.84–732401.6	18.3494	–73.4005	0.1453	0.527	0.174	0.0011	0.0002	0.922	1.460	J011324.4–732400

Continued on next page

Table A.1 – continued from previous page

Candidate	Designation	R.A.	Dec.	Error $\log \left(\frac{f_{12\mu m}}{f_{4.6\mu m}} \right)$	X $\log \left(\frac{f_{4.6\mu m}}{f_{3.4\mu m}} \right)$	Y $\times 10^{-11} \text{ erg cm}^{-2} \text{ s}^{-1}$	F_x (0.2–12 keV) $\text{erg cm}^{-2} \text{ s}^{-1}$	eF _x mag	Y – J mag	J – K _s	XMM_id
53	J011335.15–735510.3	18.3965	–73.9195	0.1505	0.524	0.335	0.0033	0.0005	0.256	1.030	-
54	J011420.98–722328.4	18.5874	–72.3912	0.1812	0.703	0.197	0.0030	0.0004	0.262	1.530	J011421.3–722327
54	J011452.86–735439.2	18.7203	–73.9109	0.1004	0.263	0.129	0.0035	0.0003	0.783	1.140	-
56	J011543.81–735002.0	18.9326	–73.8339	0.1318	0.421	0.297	0.0036	0.0003	0.611	1.300	-
57	J011606.88–731725.0	19.0287	–73.2903	0.0981	0.169	0.148	0.0038	0.0009	0.798	1.580	J011606.7–731725
58	J011732.79–735228.6	19.3867	–73.8746	0.1794	0.576	0.077	0.0042	0.0020	0.676	1.610	-
59	J011744.71–733922.1	19.4363	–73.6562	0.0977	0.451	0.086	0.0180	0.0006	0.296	1.320	J011744.7–733923
60	J011915.12–733052.9	19.8130	–73.5147	0.1280	0.520	0.300	0.0018	0.0002	0.375	1.140	J011915.0–733054
61	J012007.47–734917.6	20.0311	–73.8216	0.0905	0.447	0.035	0.0025	0.0003	0.382	0.612	-
62	J012008.63–733045.0	20.0360	–73.5125	0.1037	0.234	0.109	0.0069	0.0004	0.510	1.520	J012008.8–733044
63	J012033.96–752359.1	20.1415	–75.3998	0.1064	0.427	0.230	0.0095	0.0010	0.580	1.080	-
64	J012142.29–732051.0	20.4262	–73.3475	0.1918	0.603	0.206	0.0024	0.0004	0.470	2.280	-
65	J012149.23–724949.3	20.4551	–72.8304	0.0920	0.257	0.100	0.0069	0.0007	0.525	1.630	-
66	J012149.94–724445.2	20.4581	–72.7459	0.0940	0.372	0.016	0.0110	0.0010	0.403	1.630	-
67	J012206.29–730450.1	20.5262	–73.0806	0.0861	0.365	0.049	0.0013	0.0002	0.643	1.450	J012205.8–730447
68	J012455.51–733001.9	21.2313	–73.5005	0.2014	0.483	0.244	0.0040	0.0002	0.486	1.350	-
69	J012806.97–730824.4	22.0291	–73.1401	0.1832	0.743	0.228	0.0015	0.0002	0	0.0	-
70	J012820.97–732203.4	22.0874	–73.3676	0.1870	0.662	0.337	0.0025	0.0003	0.327	1.340	-
71	J012938.05–742144.8	22.4086	–74.3625	0.1208	0.474	0.190	0.0070	0.0010	0.218	1.240	-
72	J013028.52–730004.9	22.6189	–73.0014	0.1673	0.520	0.170	0.0013	0.0003	0	2.070	-
73	J013119.92–742505.7	22.8330	–74.4183	0.1324	0.421	0.230	0.0028	0.0005	0.520	1.020	-
74	J013206.20–733254.7	23.0258	–73.5485	0.1131	0.394	0.158	0.0026	0.0001	0.735	1.510	-
75	J013209.11–743504.9	23.0380	–74.5847	0.0619	0.157	–0.020	0.0110	0.0006	0.363	1.620	-
76	J013211.69–733621.0	23.0487	–73.6058	0.2683	0.734	0.296	0.0023	0.0003	0.718	1.750	-
77	J013254.61–743954.3	23.2276	–74.6651	0.0870	0.407	0.024	0.0071	0.0020	0.705	2.030	-
78	J013310.11–731129.9	23.2922	–73.1916	0.2723	0.795	0.179	0.0019	0.0003	0.510	1.090	-
79	J013349.39–731942.8	23.4558	–73.3286	0.2060	0.666	0.176	0.0013	0.0001	0.424	0.820	-
80	J013445.95–732005.7	23.6915	–73.3349	0.1151	0.303	0.176	0.0091	0.0005	0.745	1.130	-
81	J013607.46–741731.7	24.0311	–74.2922	0.1111	0.405	0.150	0.0120	0.0030	0.0	1.890	-

The designation, RA, Dec, associated error and the X and Y colours correspond to the ALLWISE source.

The X-ray flux and the associated error (F_x and eF_x) are from the corresponding X-ray counterpart.

Y – J and J – K_s colours are from the corresponding VISTA counterpart.

Sources where Y – J and J – K_s are 0 do not have a VISTA counterpart in the corresponding bands to compute the colours.

XMM_ids correspond to sources already included in Sturm et al. (2013b).

Table A.2: Log of the spectroscopic observations. For each object we list: name, coordinates, UT at the start of the observations, number and exposure times for individual spectra, airmass range, slit's position angle and adopted redshift.

Candidate	RA Dec (J2000)	UT at start of obs. yyyy-mm-ddThh:mm:ss	Exp. (s)	sec z (dex)	SlitPos. Ang. (deg)	Adopted Redshift
59	01:17:44.713 -73:39:22.173	2017-10-22T00:03:49	2×090	1.866–1.854	69.182	2.235±0.008
35	00:57:49.754 -71:18:02.337	2017-10-05T00:18:44	1×300	1.924–1.902	77.926	1.001±0.015
06	00:39:18.199 -73:03:31.528	2017-10-23T05:30:37	2×180	1.612–1.625	−37.557	0.345±0.001
47	01:08:49.536 -72:12:33.138	2017-10-15T00:13:28	2×210	1.870–1.843	74.465	0.432±0.002
26	00:53:26.067 -71:48:21.210	2017-10-22T00:25:36	2×270	1.690–1.666	59.565	0.982±0.015
18	00:50:57.598 -71:41:32.166	2017-10-23T05:45:16	2×300	1.582–1.603	−40.381	0.837±0.015

Table A.3: Derived line parameters from our optical spectra. For the doublet [OII] that is unresolved in our data we adopted a rest wavelength of 3727.89 Å averaging the central wavelengths of the two components in 1:2 ratio, approximately proportional to the flux ratio of the two components. The wavelength and redshift errors reflect only random uncertainties.

Candidate	Spectral features	observed wavelength (Å)	Redshift
59	CIV	5015.26±1.26	2.238±0.001
	CIII	6164.46±4.63	2.230±0.002
35	MgII	5600.17±5.47	1.001±0.002
06	[OII]	5013.71±0.05	0.345±0.001
	[NeIII]	5204.39±0.05	0.345±0.001
	H β	6537.28±0.03	0.344±0.001
	[OIII]	6670.21±0.06	0.345±0.001
	[OIII]	6734.62±0.02	0.345±0.001
47	[OII]	5341.68±0.06	0.433±0.001
	H β	6957.91±0.08	0.431±0.001
	[OIII]	7098.02±1.77	0.431±0.001
	[OIII]	7169.62±1.19	0.432±0.001
26	MgII	5546.48±1.00	0.982±0.001
18	MgII	5141.63±0.74	0.837±0.001

Table A.4: Identified candidates for obscured AGN.

Designation	R.A. °	Dec. °	Error "	$F_x(0.2-12 \text{ keV})$ $\times 10^{-11} \text{ erg cm}^{-2} \text{ s}^{-1}$	eF_x $\text{erg cm}^{-2} \text{ s}^{-1}$	HR2	HR3	HR4	XMM_id
J002523.92-712322.4	6.3497	-71.3896	0.1059	0.0065	0.0010	0.055	-0.42	0.27	-
J002606.42-711301.6	6.5267	-71.2171	0.1505	0.0042	0.0007	-0.490	-0.54	0.43	-
J002636.61-712409.5	6.6525	-71.4027	0.1365	0.0022	0.0002	0.180	-0.80	-0.06	-
J004226.41-730417.5	10.6101	-73.0716	0.0558	0.0035	0.0005	-0.200	0.03	0.43	J004226.3-730418
J004633.42-734443.2	11.6393	-73.7453	0.1022	0.0027	0.0005	0.460	-0.28	0.23	J004632.9-734444
J005231.59-704705.5	13.1317	-70.7849	0.1003	0.0047	0.0010	0.360	-0.69	0.34	J005232.3-704708
J005334.75-750404.0	13.3948	-75.0678	0.0633	0.0100	0.0020	0.063	-0.57	0.41	J005334.5-750406
J005415.32-743153.0	13.5638	-74.5314	0.1259	0.0037	0.0003	0.053	-0.54	0.19	J005415.5-743153
J005749.70-732547.0	14.4571	-73.4297	0.0433	0.0028	0.0005	0.095	-0.23	0.55	J005750.2-732542
J005859.72-711457.2	14.7489	-71.2492	0.0654	0.0079	0.0020	0.230	-0.58	0.10	J005859.7-711458
J010033.38-715037.2	15.1391	-71.8437	0.1435	0.0024	0.0005	-0.009	-0.43	0.45	J010033.4-715039
211.16703.311	15.5600	-73.2739	1	0.0054	0.0010	0.480	-0.84	0.71	-
211.16765.212	15.6450	-72.9061	1	0.0045	0.0010	0.690	-0.58	0.12	J010234.7-725425
J011420.98-722328.4	18.5874	-72.3912	0.1812	0.0030	0.0004	0.450	-0.55	0.22	J011421.3-722327
J011606.88-731725.0	19.0287	-73.2903	0.0981	0.0038	0.0009	1	-0.36	0.46	J011606.7-731725
J011732.79-735228.6	19.3867	-73.8746	0.1794	0.0042	0.0020	0.340	-0.38	0.34	-
J012024.93-734720.3	20.1039	-73.7890	0.1024	0.0030	0.0007	0.430	-0.38	0.15	-
J012938.05-742144.8	22.4086	-74.3625	0.1208	0.0070	0.0010	0.040	-0.61	0.27	-
J013119.92-742505.7	22.8330	-74.4183	0.1324	0.0028	0.0005	0.190	-0.84	0.70	-
J013254.61-743954.3	23.2276	-74.6651	0.0870	0.0071	0.0020	0.500	-0.49	0.40	-

The designation, R.A., Dec, associated error and the X and Y colours correspond to the ALLWISE or HMQ/MILLIQUAS source.

The X-ray flux and the associated error (F_x and eF_x) are from the corresponding X-ray counterpart.

HR2 HR3 and HR4 refer to the hardness ratios in the energy range of 0.5-1, 1-2 and 2-4.5 keV respectively.

XMM_ids correspond to sources already included in Sturm et al. (2013b).

Table A.5: Sample of the first five entries in the catalogue of AGN compiled from this work.

Designation	R.A. °	Dec. °	Error "	R.A. ° (X-ray)	Dec. ° (X-ray)	Error " (X-ray)	separation "	X $\log \left(\frac{f_{12\mu m}}{f_{4.6\mu m}} \right)$	Y $\log \left(\frac{f_{4.6\mu m}}{f_{3.4\mu m}} \right)$	F_x (0.2–12 keV) $\times 10^{-11} \text{ erg cm}^{-2} \text{ s}^{-1}$
J002330.72–722043.6	5.87803	–72.3455	0.0374	5.87776	–72.3455	0.341	0.29	0.454	0.046	0.2000
J002516.40–712456.4	6.31835	–71.4157	0.0986	6.31832	–71.4156	0.879	0.15	0.441	0.232	0.0088
J002523.92–712322.4	6.3497	–71.3896	0.1059	6.34863	–71.3895	1.240	1.30	0.244	0.152	0.0065
J002557.21–711617.2	6.4884	–71.2715	0.0719	6.48785	–71.2713	0.694	0.96	0.460	0.303	0.0064
J002557.82–712540.7	6.49095	–71.4280	0.0924	6.49109	–71.4283	1.160	1.20	0.391	0.076	0.0026

Designation	eF_x $\text{erg cm}^{-2} \text{ s}^{-1}$	HR1	HR2	HR3	HR4	$Y - J$ mag	$J - K_s$ mag	XMM_id	z	Identification
J002330.72–722043.6	0.0020	0.296	–0.080	–0.458	–0.504	0.617	1.35	–	–	ALLWISE
J002516.40–712456.4	0.0010	0.114	0.069	–0.155	–0.216	0.415	1.32	–	–	ALLWISE
J002523.92–712322.4	0.0010	0.330	0.055	–0.425	0.271	0.619	1.29	–	–	–
J002557.21–711617.2	0.0005	0.187	–0.080	–0.577	–0.699	0.098	1.14	–	–	–
J002557.82–712540.7	0.0004	–0.018	–0.019	–0.339	–0.183	0.748	1.32	–	–	HMQ/MILLIQUAS

Columns have the same meanings as in Tables A.1 and A.4. z refers to the redshift if known.

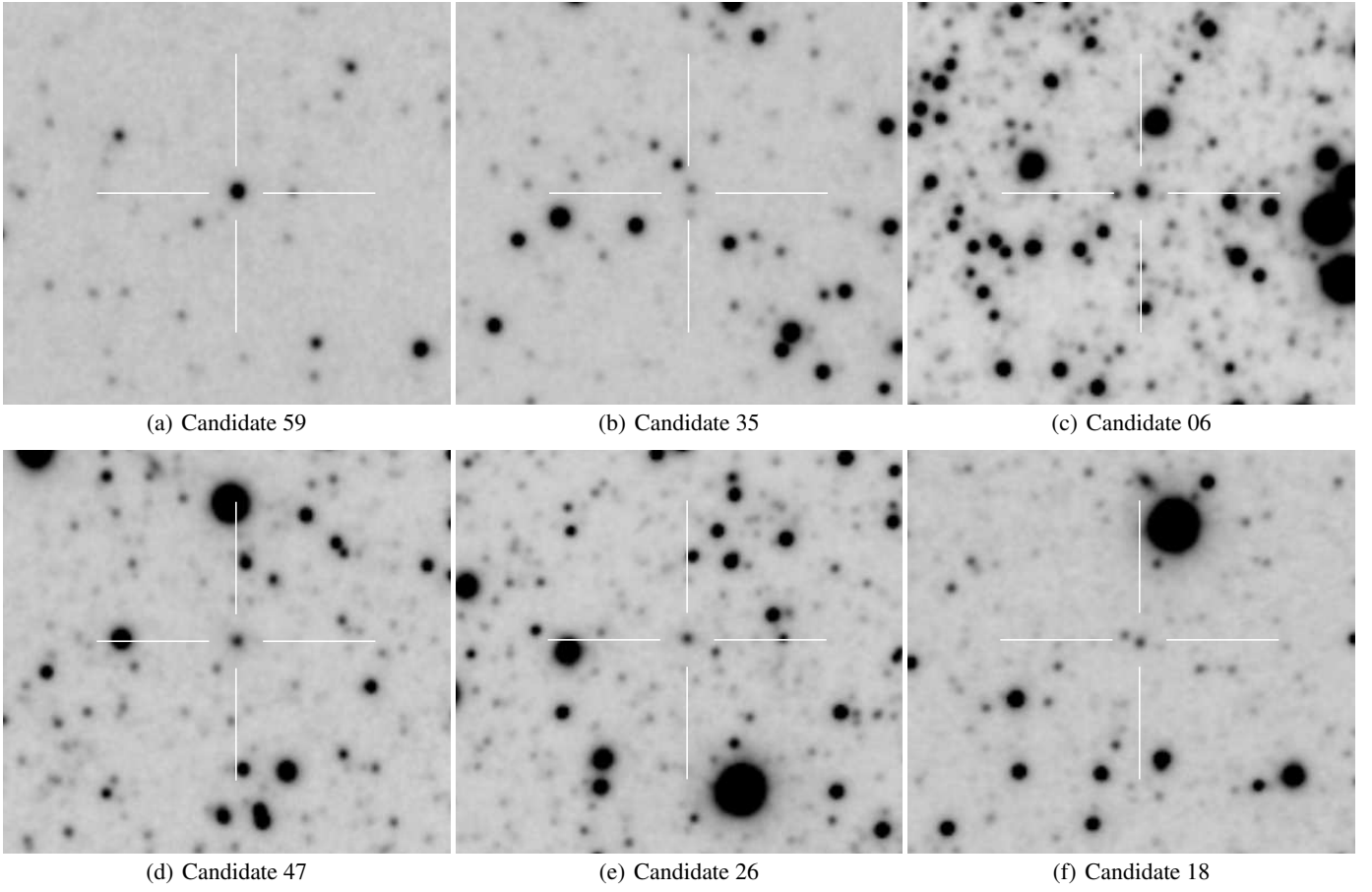


Fig. B.1: Finding charts in the Y -band for all 6 objects (crosses) with follow-up spectroscopy. The images are $1 \times 1 \text{ arcmin}^2$. North is at the top and east is to the left.

Appendix B: Figures